

# XAS Measurements of Chromium Redox in Proton Damaged Glass




Steven P. Turner  
The Department of Physics  
Aberystwyth University

A thesis submitted for the degree of  
*Master of Philosophy*

June 2017

## Mandatory Layout of Declaration/Statements

<b>Word Count of thesis:</b> DECLARATION	7604
This work has not previously been accepted in substance for any degree and is not being concurrently submitted in candidature for any degree.	
Candidate name	Steven Paul Turner
Signature:	
Date:	29. Jun. 2017

### STATEMENT 1

This thesis is the result of my own investigations, except where otherwise stated. Where **\*correction services** have been used, the extent and nature of the correction is clearly marked in a footnote(s).


Other sources are acknowledged by footnotes giving explicit references. A bibliography is appended.

Signature:	
Date:	29. Jun. 2017

[\*this refers to the extent to which the text has been corrected by others]

### STATEMENT 2

I hereby give consent for my thesis, if accepted, to be available for photocopying and for inter-library loan, and for the title and summary to be made available to outside organisations.

Signature:	
Date:	29. Jun. 2017

**NB:** *Candidates on whose behalf a bar on access (hard copy) has been approved by the University should use the following version of Statement 2:*

I hereby give consent for my thesis, if accepted, to be available for photocopying and for inter-library loans after expiry of a bar on access approved by Aberystwyth University.

Signature:	
Date:	

## **Summary of Thesis**

Surname: **Turner**

Forenames: **Steven Paul**

Degree: **MPhil**

Academic Year: **2016/2017**

Full Title of Thesis: **XAS Measurements of Chromium Redox in Proton Damaged Glass**

Summary:

Soda-lime-silicate glasses containing low concentrations of chromium have been investigated using Cr K-edge X-ray Absorption Near Edge Spectroscopy (XANES) and Extended X-ray Absorption Fine Structure (EXAFS). The synthesised glasses were bombarded with protons at 10.8 and 20MeV to induce structural damage and simulate irradiation in an extra-planetary environment. Post-irradiation, glasses containing 1.5 percent  $\text{Cr}_2\text{O}_3$  showed significant damage at high proton energy, which presented as an increase in the  $\text{Cr(VI)}/\text{Cr}_{\text{total}}$  ratio. Bond distances for Cr(III)-O and Cr(VI)-O were calculated from the fitting of experimental EXAFS data.

## Acknowledgements

I would like to thank Dr Martin Wilding, and Professor Andy Evans for the opportunity to conduct this research. Special thanks must go to Dr Dave Langstaff for his help and guidance during the writing of this document. Thanks also to my friends in the office, Morgan, Rachel, and Simon for laughs and support. Thanks also go to Dr Mali Balasubramanian at the Advanced Photon Source for his assistance and excellent guidance during the XANES measurement at beamline 20-BM-B, and to Dr Gordon Allison for his assistance with the FTIR study. Finally, thank you to Charlotte, for her support, encouragement and patience, and to my family, for theirs.

This project was funded by the Knowledge Economy Skills Scholarship (KESS)

## Abstract

Soda-lime-silicate glasses containing low concentrations of chromium have been investigated using Cr K-edge X-ray Absorption Near Edge Spectroscopy (XANES) and Extended X-ray Absorption Fine Structure (EXAFS). The synthesised glasses were bombarded with protons at 10.8 and 20MeV to induce structural damage and simulate irradiation in a extra-planetary environment. Post-irradiation, glasses containing 1.5 percent Cr<sub>2</sub>O<sub>3</sub> showed significant damage at high proton energy, which presented as an increase in the  $\Sigma \text{Cr(VI)}/\text{Cr}_{total}$  ratio. Bond distances for Cr(III)-O and Cr(VI)-O were calculated from the fitting of experimental EXAFS data.

# Contents

<b>1</b>	<b>Introduction to Thesis</b>	<b>1</b>
<b>2</b>	<b>Introduction</b>	<b>3</b>
2.1	Glass Structure . . . . .	3
2.2	Causes of Colour in Glass . . . . .	3
2.2.1	Chromium Environment in Silicate Glass . . . . .	4
2.3	Cyclotrons . . . . .	5
2.4	Synchrotrons and X-rays . . . . .	6
2.4.1	History of X-rays . . . . .	6
2.4.2	Synchrotrons . . . . .	6
2.4.3	Monochromators . . . . .	7
2.5	X-ray Absorption Spectroscopy . . . . .	8
2.5.1	Absorption Mechanism . . . . .	8
2.5.2	XAS Experimental Configurations . . . . .	9
2.5.3	EXAFS . . . . .	11
2.5.4	XANES . . . . .	11
2.6	Fourier Transform Infrared Spectroscopy (FTIR) . . . . .	12
<b>3</b>	<b>Proton Radiation Damage to Cr Containing Glass</b>	<b>13</b>
3.1	Sample Synthesis . . . . .	13
3.1.1	Starting Materials . . . . .	13
3.1.2	Synthesis of Glass Samples . . . . .	14

3.1.2.1	Primary Melt . . . . .	14
3.1.2.2	Secondary Melt . . . . .	15
3.1.2.3	Final Melt . . . . .	15
3.1.3	Sample Fabrication . . . . .	16
3.1.3.1	Core Cutting . . . . .	16
3.1.3.2	Slicing . . . . .	16
3.1.3.3	Final Finishing . . . . .	17
3.2	X-ray Diffraction . . . . .	17
3.3	Proton Irradiation . . . . .	18
3.4	XANES of HCr, MCr and LCr samples . . . . .	18
3.5	FTIR . . . . .	21
<b>4</b>	<b>Results</b>	<b>23</b>
4.1	XRD . . . . .	23
4.2	XANES . . . . .	24
4.2.1	Data Processing . . . . .	24
4.2.2	Pre-edge of HCr Sample Set . . . . .	25
4.2.3	Pre-edge of MCr Sample Set . . . . .	26
4.2.4	Pre-edge of LCr Sample Set . . . . .	26
4.2.5	EXAFS . . . . .	28
4.3	FTIR . . . . .	28
<b>5</b>	<b>Discussion</b>	<b>31</b>
5.0.1	XAS of HCr, MCr and LCr . . . . .	31
5.0.1.1	HCr . . . . .	31
5.0.1.2	MCr and LCr . . . . .	32
5.0.2	FTIR . . . . .	34

<b>6 Conclusion</b>	<b>35</b>
6.1 Further Work . . . . .	36
<b>A FTIR</b>	<b>37</b>
<b>B XRD</b>	<b>38</b>
<b>C EXAFS</b>	<b>40</b>
<b>D XAS Noise</b>	<b>44</b>
<b>Bibliography</b>	<b>47</b>



# List of Figures

2.1	Amorphous SiO <sub>4</sub> . . . . .	4
2.2	Diagram of a typical Cyclotron . . . . .	6
2.3	Top-down View of Experimental Setup . . . . .	10
2.4	Example XAS spectra . . . . .	11
3.1	Beam Dimensions Relative to the Sample . . . . .	19
3.2	Main Experimental Setup . . . . .	20
3.3	Top-down View of Experimental Setup . . . . .	20
4.1	X-ray Diffractogram for HCr01 sample after final stage of synthesis . . . . .	23
4.2	Initial raw data processing method for HCr01 . . . . .	24
4.3	HCr Pre-edge XANES spectra . . . . .	25
4.4	Fit of HCr01 and HCr05 pre-edge . . . . .	26
4.5	MCr Pre-edge XANES spectra . . . . .	27
4.6	LCr Pre-edge XANES spectra . . . . .	27
4.7	Chromium K-edge experimental k <sup>3</sup> -weighted EXAFS and fit for HCr01 . . . . .	29
4.8	FTIR Spectra for the HCr sample set . . . . .	29
4.9	FTIR Spectra for the MCr sample set . . . . .	29
4.10	FTIR Spectra for the LCr sample set . . . . .	30
5.1	MCr01 chart showing difference between individual scans and the average of all six scans . . . . .	33

A.1	Background Spectra for subtraction during FTIR scans . . . . .	37
B.1	X-ray Diffractogram for MCr01 sample after final stage of synthesis .	38
B.2	X-ray Diffractogram for LCr01 sample after final stage of synthesis .	39
C.1	Cr K-edge experimental $k^3$ -weighted EXAFS and fit (smooth line) for HCr01 and HCr02. . . . .	40
C.2	Cr K-edge experimental $k^3$ -weighted EXAFS and fit (smooth line) for HCr03 and HCr04. . . . .	40
C.3	Cr K-edge experimental $k^3$ -weighted EXAFS and fit (smooth line) for HCr05. . . . .	41
C.4	Cr K-edge experimental $k^3$ -weighted EXAFS and fit (smooth line) for MCr01 and MCr02. . . . .	41
C.5	Cr K-edge experimental $k^3$ -weighted EXAFS and fit (smooth line) for MCr03 and MCr04. . . . .	41
C.6	Cr K-edge experimental $k^3$ -weighted EXAFS and fit (smooth line) for MCr05. . . . .	42
C.7	Cr K-edge experimental $k^3$ -weighted EXAFS and fit (smooth line) for LCr01 and LCr02. . . . .	42
C.8	Cr K-edge experimental $k^3$ -weighted EXAFS and fit (smooth line) for LCr03 and LCr04. . . . .	42
C.9	Cr K-edge experimental $k^3$ -weighted EXAFS and fit (smooth line) for LCr05. . . . .	43
D.1	Averaged $\mu(E)$ vs Energy minus Individual Scan $\mu(E)$ vs for the HCr sample set. . . . .	44
D.2	Averaged $\mu(E)$ vs Energy minus Individual Scan $\mu(E)$ vs for the MCr sample set. . . . .	45

D.3 Averaged $\mu(E)$ vs Energy minus Individual Scan $\mu(E)$ vs for the LCr sample set. . . . .	46
--	----

# List of Tables

3.1	Pre-melt mixture composition of base glass before doping with Chromium Oxide . . . . .	14
3.2	Summary of the synthesis regime for HCr, MCr and LCr samples . . .	16
3.3	Proton doses for Silicate Glass Samples . . . . .	18
4.1	Bond distances for the HCr Sample set . . . . .	28
5.1	Integrated Total Area under the pre-edge peak . . . . .	32

# Chapter 1

## Introduction to Thesis

The purpose of this report is to display the work carried out towards understanding the causes of colour in silicate glass caused by chromium, and how it is affected by proton radiation.

Silicate glasses of various compositions have long been used in a wide range of applications for their optical and thermal properties. Recently, glasses that have been damaged by radiation (including, X-rays, neutrons, ultraviolet, protons and  $\gamma$ -rays) have been investigated for use on spacecraft. PanCam[1] is an instrument being developed for deployment to the Mars surface, for the purpose of multi-spectral imaging. PanCam requires a calibration target - an array of 8 coloured glass discs to provide a reference for multi-spectral imaging. In preliminary tests, some glass targets showed resistance to proton radiation, but glasses doped with Cr and Fe showed a change in optical transmission post-radiation. These glasses therefore seem ill-suited for use as calibration targets, but if the optical changes can be predicted, then the in-situ calibration may be able to take this into account on the Martian surface.

In the first part of this thesis, the causes of colour and a general background of silicate glasses are discussed. The operation of cyclotrons and synchrotrons, and the technique of X-ray absorption spectroscopy are briefly explained. Following on from this, sample synthesis is described in detail, as are the methods of how the samples were brought down to final dimensions.

This work would not have been possible without the use of the Advanced Photon Source synchrotron in Chicago. A 72 hour beamtime for March 2014 was awarded after a successful proposal submitted in December 2013. This allowed the necessary experiments to gather XANES and EXAFS data to be carried out, with the assistance of the beamline staff. Prior to the beamtime, the samples were irradiated with protons at Birmingham University, UK, one week before the beamtime began. A post-beamtime investigation using Fourier Transform Infrared Spectroscopy was carried out to further compare the irradiated samples with a un-irradiated sample was performed soon after the beamtime at Aberystwyth University, in the Department of Biological, Environmental, and Rural Sciences (IBERS) with the help of the department's staff.

# Chapter 2

## Introduction

### 2.1 Glass Structure

”Glass” is a term given to a broad range of materials, with amorphous, or non-crystalline atomic structure. Silicate glasses have a base constituent of tetrahedral  $\text{SiO}_4$  units, that are connected in a manner that exhibits no crystalline order over long range. However, it can be said that there is some order to the network, as each silicon atom is coordinated with 4 oxygen atoms, and the Si-O bond length has a narrow distribution across the whole network. Figure 2.1 shows an example of amorphous  $\text{SiO}_4$  in two dimensions. Each Si atom is bonded to 4 oxygen atoms (only 3 are shown as the fourth is above or below the plane in the figure).

Network modifiers are added to the composition of glass in order to decrease the overall network of the glass. For example, in soda-lime-silicate glasses, the addition of calcium (as  $\text{CaO}$ ) breaks oxygen bridges between Si atoms, and forms Non-Bridging Oxygens, or NBO [3]. This reduces the strength of the glass structure, and lowers viscosity and melting temperature.

### 2.2 Causes of Colour in Glass

One of the main causes of colour in silicate glasses is the inclusion of chromophores, or dopants, often transition metals, within the glass matrix. These large cations

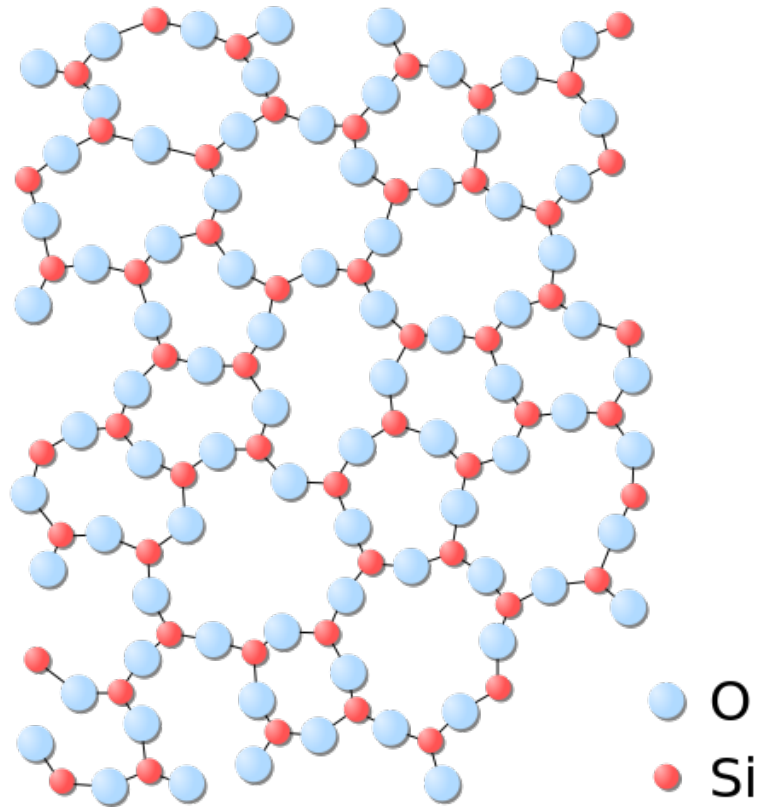


Figure 2.1: Amorphous  $\text{SiO}_4$ . Each Si atom is coordinated with 4 oxygen atoms, with the fourth above or below the plane of view[2].

have absorption bands that can be easily detected using optical techniques (such as transmission spectroscopy) and are generally characteristic of the dopant species. For instance, iron will impart a soft green colour to silicate glass, but the next element in the periodic table - cobalt - imparts deep blue. Further to this, the resulting colour of the glass can be dependent on the valence states of the dopant metal during synthesis[4].

### 2.2.1 Chromium Environment in Silicate Glass

Previous investigations of chromium in silicate glasses show that  $\text{Cr}^{3+}$  (Cr(III)) occurs in weakly distorted octahedral sites, accompanied by tetrahedral  $\text{Cr}^{6+}$  (Cr(VI)). Optical techniques to determine the relative amounts of these cations can be used, such as transmission spectroscopy, but information may be concealed by an overlap of



the absorption bands [5]. However, there are many reports that use X-ray techniques to reveal information on the oxidation state of chromium, as well as information on the local structure around the absorber atom [6, 7, 8, 9, 10, 11]. X-ray Absorption Spectroscopy is a powerful technique that can be used to determine the relative and quantitative (providing a reference sample with known amounts of  $\text{Cr}^{3+}$  and  $\text{Cr}^{6+}$  is used for comparison) amounts of the two valence states in a sample.

## 2.3 Cyclotrons

The production of a beam of protons can be achieved with the use of a Cyclotron, a type of particle accelerator still used today in the physical sciences, and in particular, nuclear medicine (they are used to produce short-lived isotopes for PET imaging). Invented in 1932 by Ernest O. Lawrence at the University of California, Berkeley, Cyclotrons were the most powerful forms of particle accelerators available until the invention of Synchrotrons in the 1950s. Their principle of operation is to accelerate a charged particle beam using two electrodes with a high frequency alternating voltages applied, in a vacuum. Figure 2.2 shows the general setup and principle of operation of a Cyclotron.

The two electrodes are hollow D shapes made from sheet metal (called Dees), which allows the particle beam to pass through them. The particles are injected into the centre of the Cyclotron, and an alternating voltage causes the particles to be accelerated towards the Dee that does not contain the particles. As the particles cross the gap between the two electrodes, the voltage reverses and the particles continue to accelerate in a spiral path towards the outside of the cyclotron. Above and below the vacuum chamber containing the Dees, two large magnets provide a field to bend the particles in a curved path due to the Lorentz force.

The protons are ejected through a window and pass through an ionisation chamber which measures the charge caused by the beam, with the beam directed towards the

sample.

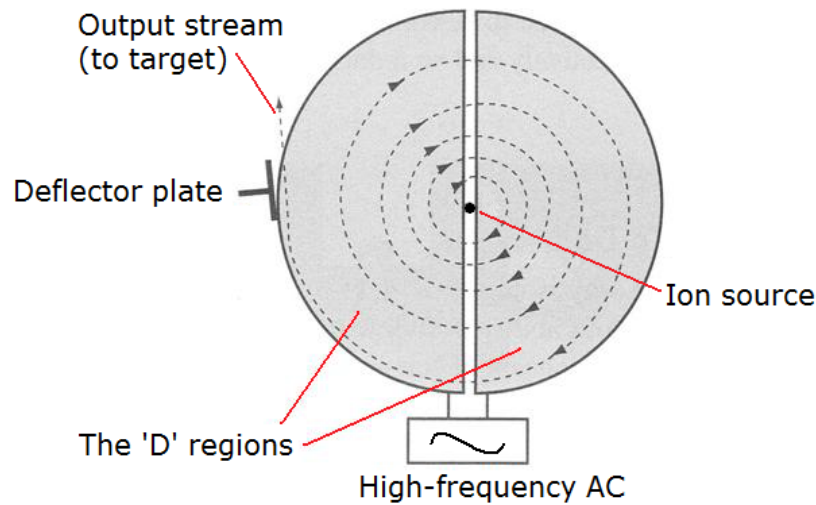


Figure 2.2: Diagram of the Cyclotron[12].

## 2.4 Synchrotrons and X-rays

### 2.4.1 History of X-rays

The region of the electromagnetic spectrum now known as X-rays was first discovered by Wilhelm Röntgen in 1895, with the first X-ray radiogram *Hand mit Ringen* being presented on the 22 December 1895. In the years following Röntgen's discovery, notable scientists such as William Crookes, Hermann von Helmholtz, Max von Laue and Nikola Tesla worked on the mathematics and the experimental applications of X-rays, laying the groundwork for important techniques such as fluorescence and luminescence, and of course medical imaging. In the past 50 or so years, X-ray Absorption Spectroscopy (XAS) has made contributions to a wide range of topics in various fields[13].

### 2.4.2 Synchrotrons

The main part of this study requires the use of a tuneable X-ray source to probe the local structure of Cr in the glass matrix. To do this, the Synchrotron facility

at the Advanced Photon Source (APS, located at the Argonne National Laboratory, Chicago, Illinois, USA[14]) was used to perform X-ray Absorption Spectroscopy. A synchrotron is another type of particle accelerator that was designed to overcome the limitations of the cyclotron caused by relativistic particle speeds. Instead of the radius of the particle path increasing with energy, and a fixed RF electric field, a synchrotron uses a fixed radius and a pulsed RF field to accelerate electrons. They are contained in an evacuated storage ring (with a radius ranging from metres (for MeV energies) to kilometres (TeV) and are accelerated in accelerating cavities by an RF oscillator that provides an energy boost. The particle beam within the accelerating cavity is straight, but large bending magnets are used to curve the beam within the storage ring.

### **2.4.3 Monochromators**

X-rays are produced in synchrotron facilities by electrons travelling at relativistic speeds on a curved path. At experimental facilities around the world, a storage ring has several beamlines that allow an X-ray beam to exit tangentially to the storage ring and each beamline will cover a specific range of photon energies. A monochromator is used to select a specific energy, and adjustment of the monochromator allows a spectrum to be produced. Monochromation of an X-ray beam works on the principle of Bragg diffraction, where a crystal lattice diffracts an incoming beam of light at wavelengths that obey Braggs Law for the particular lattice spacing  $d$  of the crystal. The regularity of a crystal lattice allows for the coherent scattering of light due to constructive interference at certain angles. The incoming beam is diffracted, and based on the lattice spacing, there is a difference in the path length travelled by the beam. Constructive interference occurs when the difference in path length is such that the diffracted beams are in phase, and so strong Bragg peaks are observed. With an incoming beam of white light, a monochromatic diffracted beam will be produced,

with a wavelength that depends on the angle of the crystal lattice with respect to the incoming beam. Adjustment of the angle changes the effective lattice spacing, and a wavelength can be selected provided the angle of the monochromator can be finely controlled. For example, the beamline used in this study - 20-BM-B at the Advanced Photon Source[14] - uses a silicon crystal monochromator in the 111 plane (which provides the largest d spacing in silicon  $3.136\text{\AA}$ ). Using the Bragg condition:

$$n\lambda = 2d\sin\theta \quad (2.1)$$

Where  $\lambda$  is the monochromatic X-ray wavelength,  $n$  is the diffraction order (usually equal to 1 in this case) and  $\theta$  is the angle of incidence of the unmonochromated white beam, the required angle for selecting a particular wavelength of X-ray can be calculated. For the Chromium K edge at 5989 eV ( $\lambda= 0.20702\text{nm}$ ), the required monochromator angle would be 19.273 degrees with respect to the incoming beam.

## 2.5 X-ray Absorption Spectroscopy

The development of synchrotron sources over the last few decades has led to advances in our ability to probe condensed matter with increasing accuracy and complexity. Synchrotrons can be used for a wide variety of X-ray based techniques including Wide and Small Angle X-ray Scattering, Diffraction, and Tomography. One of the most useful tools for probing the atomic structure of materials is XAS[15].

### 2.5.1 Absorption Mechanism

X-rays interact with matter through different mechanisms, including the photo-electric effect, fluorescent emission, and Auger processes. In the photo-electric effect, the X-ray photon is absorbed by a core electron in the absorbing atom. If the X-ray energy is lower than the binding energy of the core electron, then the electron will not absorb the photon, however if the X-ray energy is greater than or equal to the binding energy,

the X-ray may be absorbed and the electron will be liberated from the core level to the continuum. In this case, any energy remaining from the difference between the binding and X-ray energy is given to a photo-electron that is emitted from the atom.

This process leaves a core hole in the electronic structure of the atom, and from this excited state the atom undergoes a relaxation process where a higher level electron undergoes a transition to a lower level. This causes an emission of an X-ray photon with energy equal to the energy difference of the two states involved in the transition. This process is called fluorescence.

The point at which the X-ray energy is equal to the binding energy of the core electron can clearly be seen on a XAS spectra (see figure 2.4.). The sharp rise in absorption indicates this point and is known as the absorption edge, which corresponds to the excitation of the core electron to the continuum.

## 2.5.2 XAS Experimental Configurations

In XAS measurements, the local structure of an atom (known as the absorber) can be determined, and XAS experiments can be carried out in two similar configurations - transmission mode, and fluorescence mode. In transmission XAS, tuneable X-rays of intensity  $I_0$  are targeted on a sample material, and the absorption coefficient as a function of energy  $\mu(E)$ , based on the beam intensity after the sample ( $I_T$ ), is measured. This is based on Beers Law, where intensity of the absorbed beam is given by (assuming no reflection or refraction):

$$I_T = I_0 e^{-\mu x} \quad (2.2)$$

Where  $I_0$  is the initial beam intensity in front of the sample,  $I_T$  is the beam intensity after absorption, at distance  $x$ . Rearranged to find  $\mu(E)$  gives:

$$\mu(E) = \frac{-\ln\left(\frac{I_T}{I_0}\right)}{x} \quad (2.3)$$

Transmission XAS is a technique based on the count of the primary absorption mechanism of X-rays absorbed by core electrons.

Fluorescence XAS is used for samples that may have a low concentration of absorber (ie. the element to be probed). It is based on the secondary emission of X-ray photons following the relaxation of an electron from a higher state to a core hole left by an electron ejected by the primary X-ray absorption. In this configuration, photons are counted by a detector which is perpendicular to the incoming beam, with the samples at 45 degrees to both (an example of this geometry can be seen in Figure 2.3).



Figure 2.3: Top-down view of the sample holder and configuration of the samples with respect to the beam and detector

An XAS experiment is concerned with measuring  $\mu(E)$  below, at, and above the absorption edge, and the spectra can indicate the coordination number, valence, and bond distances around the absorber. It also has the advantage of not requiring a crystalline sample, and so is useful for probing amorphous materials and organics.

An XAS spectrum can be broken down into two main regimes, with variants of XAS techniques used to specifically probe a particular part of the absorption edge. Extended X-ray Absorption Fine Structure (EXAFS) pertains to the post-edge region

of the spectrum, and has characteristic oscillations of  $\mu(E)$  for hundreds of eV past the edge 2.4.

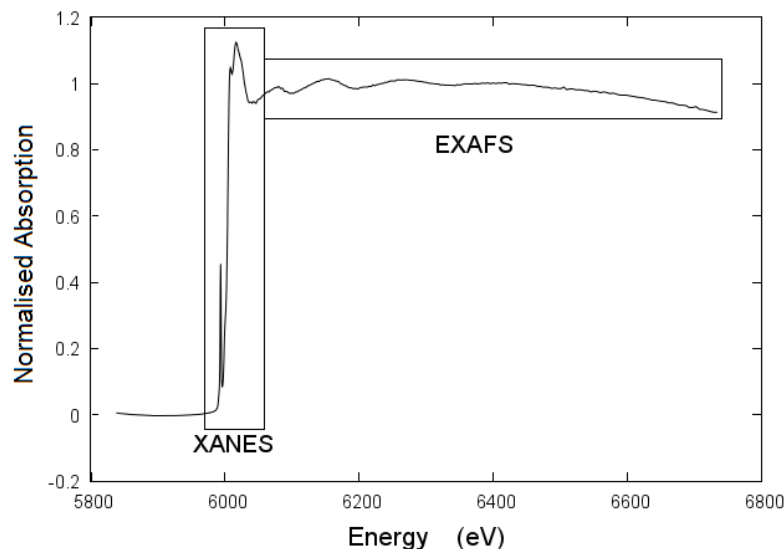


Figure 2.4: Schematic of an example XAS spectra at the Chromium k edge

### 2.5.3 EXAFS

Extended X-ray Absorption Fine Structure (EXAFS) is a technique that focuses on the post-edge region of the XAS spectra, and analysis of this area reveals information about the local structure around the absorber atom[16]. From roughly 50 to 1000 eV above the edge, small oscillations in  $\mu(E)$ , called the *fine structure* are observed. These oscillations arise from photoelectrons that are ejected from the absorber atom interacting with electrons of atoms that surround the absorber. The ejected photoelectron acts as a secondary probe (the initial probe being the X-ray photon from the synchrotron).

### 2.5.4 XANES

X-ray Absorption Near Edge Structure applies to the region of the XAS spectra that contains the edge, and pre-edge, and XANES analysis can be used to determine the

valence of the absorber atom, and the relative ratio of valences in the sample. For example, Iron in basaltic glasses exhibit a pre-edge doublet, where the relative height of each peak in the doublet is dependent on oxygen fugacity during synthesis [17]. The position in energy of the centre of the pre-edge peaks indicates the valence of the absorber, and the ratio of oxidised to reduced iron can be calculated [18] [19]. In glasses that contain transition metals, the pre-edge peak is attributed to transitions between bound electronic states such as ( $1s \rightarrow 3d$ ) [10].

## 2.6 Fourier Transform Infrared Spectroscopy (FTIR)

Fourier Transform Infrared Spectroscopy (FTIR) [20] is a common technique used to obtain absorption or emission spectra of a material, in the infrared range. FTIR spectroscopy is often used to identify unknown materials due to the unique spectra associated with the molecular structure of the sample. It can also be used to identify bond pairings, and individual molecular components of a material.

In most FTIR instruments, an interferometer is used in place of a grating or prism (like those used in dispersive spectrometers, for example, in optical spectroscopy), which allows spectra to be collected at all frequencies simultaneously, often with high spectral resolution. This non-destructive technique is advantageous due to having a fast acquisition speed, of the order of seconds. A fourier transform is applied to the interferogram, which results in a Intensity vs Frequency spectrum.



# Chapter 3

## Proton Radiation Damage to Cr Containing Glass

This chapter describes in detail the process of sample synthesis and processing used to manufacture the samples needed for the study. All samples were produced by the author at Aberystwyth University's Department of Physics.

### 3.1 Sample Synthesis

#### 3.1.1 Starting Materials

The investigated glasses were prepared using a melt-quench method. Reagent grade silicon dioxide (99.9%), calcium carbonate ( $\geq 99\%$ ) and sodium carbonate monohydrate ( $\geq 99.5\%$ ) were mixed with varying amounts of Chromium (III) Oxide  $\text{Cr}_2\text{O}_3$  ( $\geq 99.9\%$ ). The compositions by mass of the pre-melt mixtures, before doping with  $\text{Cr}_2\text{O}_3$  are shown in table 3.1. The pre melt powders were weighed using an analytical grade balance with readability of 0.1mg. Three sets of glasses were produced, each with 5 samples - the sets were designated **HCr**, **MCr** and **LCr** each with a numerical suffix (01-05) to identify an individual sample. HCr, MCr and LCr samples contained (pre-melt) 0.2016, 0.1344 and 0.0672 grams of  $\text{Cr}_2\text{O}_3$  respectively.

Compound	Base Glass Composition (g)
SiO <sub>2</sub>	6.8730
CaCO <sub>3</sub>	1.9520
Na <sub>2</sub> .CO <sub>3</sub> .H <sub>2</sub> O	4.5160

Table 3.1: Pre-melt mixture composition of base glass before doping with Chromium Oxide

### 3.1.2 Synthesis of Glass Samples

Sample synthesis consisted of three main stages - the primary and secondary melt, followed by the final ingot melt. Due to the constraints of the size of the Pt crucible (30mm diameter by 50mm height) and the size of the furnace, multiple batches of each melt were made. Each batch was then pulverised after the quench, and then mixed together thoroughly to form a main batch for the next melt.

A Platinum crucible, and a Platinum-Gold alloy crucible was used to minimise reaction with the glass melt to improve homogeneity[21]. The Pt-Au crucible was used to ease removal of the final ingot from the crucible.

#### 3.1.2.1 Primary Melt

The mixtures were first dehydrated at 120°C in a drying oven for 1 hour, in order to remove as much water as possible. H<sub>2</sub>O in the glass matrix can lead to a suppression of colour centre expression, and can affect the optical properties of the synthesised glasses[22]. These initial mixtures were dehydrated in a platinum crucible.

The mixtures were then transferred in the platinum crucible to an air tube furnace at 900°C for 24 hours. The purpose of this stage of synthesis was to decarbonate the mixture, in order to prevent the formation of carbon dioxide within the melt, which can cause the melt to foam in the furnace[4].

The glasses were then melted at 1500°C for 2 hours. Upon removal from the furnace, the melt was immediately quenched in a large volume of cold water until completely cooled. The glass was then removed from the Pt crucible and pulverised

to a fine powder.

In total, four individual batches were melted for each set of samples, totalling 12 runs. The HCr glasses were prepared first in this primary stage, followed by MCr and then LCr. Following the completion of each set, the Pt crucible was etch cleaned in room temperature Hydrofluoric Acid (HF, 48% by weight in  $H_2O$ ). The crucible was placed in a PTFE beaker, in a fume cupboard, and left for 24 hours to prevent cross-contamination from one set of samples to another.

### **3.1.2.2 Secondary Melt**

The secondary melt was to further improve the homogeneity of the samples. One quarter of the pulverised glass from the primary melt was transferred back to the cleaned platinum crucible, and then placed back in the drying oven at 120°C for 1 hour.

The crucible was then moved to the tube furnace at 900°C for 1 hour. Following this, the glasses were then melted at 1500°C for 2 hours and then removed and immediately quenched in water. The glass was removed from the crucible once it had cooled, then pulverised to a fine powder.

As with the primary melt, 4 batches of each sample set were made during the secondary melt run, totalling 12 melts. The crucible was again cleaned between sets.

This pulverisation-melt process was repeated twice more, in order to improve homogeneity and minimise the possibility of the glass samples containing crystallites.

### **3.1.2.3 Final Melt**

The pulverised glasses were then finally melted in one quarter batches in a platinum-gold crucible at 1400°C for 1 hour. Upon removal from the furnace, the crucible and melt were allowed to cool to room temperature, without quenching in water. This produced an ingot of glass with a thickness of roughly 10mm thick and 20mm in diameter at it's narrowest.

	Primary Melt	Secondary Melt	Final Melt
Dehydration Time (120 °C)	1 hour	1 hour	N/A
Decarbonation Time (900 °C)	24 hours	1 hour	N/A
Melt Time (1500 °C)	2 hour	2 hour	1 hour
Number of Batches per sample	4	4	4
Number of repeats of run	1	3	1

Table 3.2: Summary of the synthesis regime for HCr, MCr and LCr samples

### 3.1.3 Sample Fabrication

From the glass synthesis process, 12 ingots were produced, 3 of each set. These ingot were sliced, ground and polished to produce a set of 'discs', from which 5 were chosen as final samples. This section describes the processing of the ingots to samples.

#### 3.1.3.1 Core Cutting

This ingot was first secured to a holder of sacrificial perspex with epoxy glue to provide a means of safely manipulating the ingot. A cylinder with a 16mm diameter was cut from the centre of the ingot using a pillar drill with a core cutter bit. The bit was constantly water cooled and set at a low tooling speed to minimise the possibility of the ingot shattering during this process.

#### 3.1.3.2 Slicing

This cylinder was then mounted horizontally in a water cooled wafering cutter, and a shallow cut was made on the top of the cylinder to provide a flat reference face. The ingot was then cut into slices 1.5mm thick, using a 1mm thick diamond edged wafering blade. This produced on average 4 slices per ingot (on some occasions, the disc being cut broke). Each cut was made of the span of several hours, as the blade was left to cut using only gravity to grind through the cylinder.

### 3.1.3.3 Final Finishing

The cut discs were placed in a holder that mounted in a mechanical polisher. The holder pressed against a rotating plate coated in silicon carbide powder and water, which ensured that the surface of the sample was ground evenly.

The samples were ground with increasingly finer grades of silicon carbide powder, starting at 80 followed by 120, 200 then finally 400 grit. This allowed the samples to be brought to a final thickness before finishing with a final polish using zinc oxide powder mixed with water. The final thickness of the samples were  $1.00 \pm 0.01$ mm, measured with a micrometer.

Finally, 5 samples of each set were selected based on the integrity of the edges of the sample after polishing, as some had chipped slightly during the fabrication process.

Overall, sample synthesis and fabrication took between 3 and 4 months. The process was slowed by breakdowns of the furnace (including a need to replace the element array). Synthesis took around 2.5 months in total, with fabrication taking a month, as the cutting of each slice took several hours, sometimes overnight.

## 3.2 X-ray Diffraction

In order to confirm the absence of any crystalline phases in the synthesised glasses, discarded samples from the final sample fabrication were re-pulverised and X-ray Powder Diffraction was performed at Aberystwyth University Department of Physics, using a copper  $k\text{-}\alpha$  source Bruker D8 Discover with a VANTEC 500 detector. Spectra were collected over a  $2\Theta$  range from 10 to 90 degrees, with a resolution of 0.0072 degrees. An absence of sharp peaks in the diffractogram indicates that there are no crystallites present and that the sample is indeed of a glassy nature[23].

### 3.3 Proton Irradiation

Proton energies were selected based on their penetration depth, calculated using the Stopping Range of Ions in Matter (SRIM)[24]. Energies of 10 and 20 MeV were chosen - protons at 10MeV will stop within the sample (all energy from the protons deposited in the sample), and at 20 MeV, the protons pass through the sample. Each sample was irradiated at the Birmingham MC40 Cyclotron facility at the University of Birmingham Department of Physics. The MC40 Cyclotron has a maximum magnetic field of approximately 1.8 Tesla, and the adjustment of this field give a proton energy range of 11 to 38 MeV [25].

Due to the limitations of the cyclotron itself, the lowest possible energy protons that could be produced was at 10.8 MeV. Table 3.3 shows the proton energy and dose that each sample recieved.

Sample Name Suffix	Proton Energy (MeV)	Dose (Protons per cm <sup>2</sup> )
01	Unirradiated	N/A
02	10.8	1x10 <sup>11</sup>
03	10.8	3x10 <sup>11</sup>
04	20	1x10 <sup>11</sup>
05	20	3x10 <sup>11</sup>

Table 3.3: Proton doses for Silicate Glass Samples

### 3.4 XANES of HCr, MCr and LCr samples

Chromium K-edge X-ray absorption spectra were collected at beamline 20-BM-B at the Advanced Photon Source (APS) at Argonne, Illinois, USA. Data were recorded at room temperature in fluorescence detection mode using a Canberra Industries liquid nitrogen cooled multi-element germanium detector[14]. The beam dimensions were 1mm vertical by 8mm horizontal with a flux of 5x10<sup>9</sup> photons per second and a typical

energy resolution ( $\Delta E/E$ ) of  $1.4 \times 10^{-4}$ . The beam dimensions relative to the sample are shown in Figure 3.1.

These beam dimensions were chosen to allow multiple sites to be probed on the sample. Between 4 and 6 scans were made of each sample, moving the beam between 6 separate locations from scan to scan, so that no part of the sample was exposed to the incoming beam for more than 1 scan. In Figure 3.1, the beam position shown was considered to be 'position 1', with the sample move incrementally by 1mm vertically for the subsequent scans. The reasons for this method are discussed in Section 4.2.

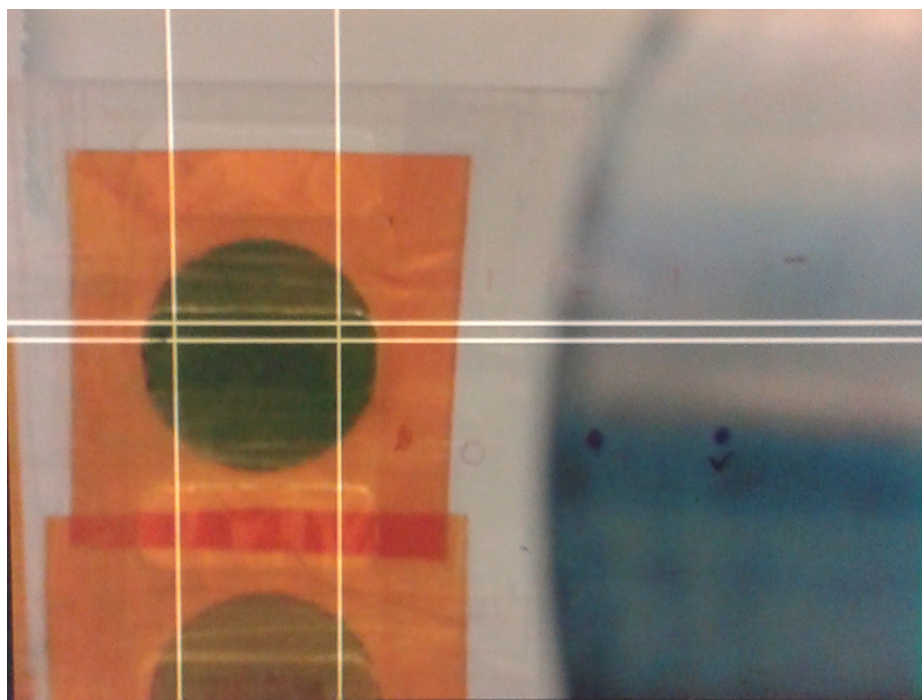


Figure 3.1: "Letterbox" beam dimensions relative to the sample

Figure 3.2 shows the experimental set up at Beamline 20-BM-B. The X-ray beam is delivered through the vacuum chambers entering the experimental enclosure from the right hand side of the figure. The samples are secured on a perspex holder perpendicular to the bench, with the holder positioned at 45 degrees to the incoming beam. The detector, and more detail of the geometry of the setup, can be seen in Figure 3.3. The detector is at the top of the figure, perpendicular to the incoming

beam, the standard configuration for XAFS fluorescence detection.

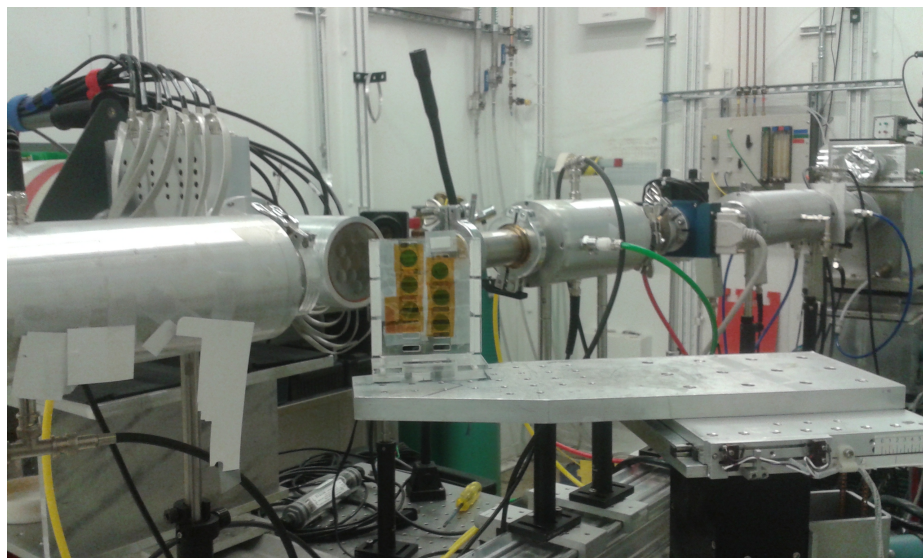


Figure 3.2: The experimental configuration used at beamline BM20-B



Figure 3.3: Top-down view of the sample holder and configuration of the samples with respect to the beam and detector

In Figures 3.1, 3.2 and 3.3, the samples are shown to be coated in Kapton tape individually, prior to being mounted on the holder. Upon arrival at the APS, the samples were swabbed and tested for radioactivity, and were sealed in Kapton as a precaution, due to the samples having been irradiated with protons. Whether the



samples were radioactive or not is unknown, as the results of the testing done prior to the beamtime were not provided. Kapton tape was considered an acceptable solution as it is radiation resistant and transparent to X-rays [26], so it would not effect the XAFS experiment.

Energy calibration was made with respect to the first inflection point in metal Cr, which was determined to be 5989.0 eV. A spacing of 0.2eV in the XANES region (5975 to 6030eV) and  $0.05\text{\AA}^{-1}$  to  $k = 14\text{\AA}^{-1}$  in the EXAFS were used during data collection, with a dwell time of 2 seconds.

### 3.5 FTIR

To compare the individual samples across all sets to each other, Fourier Transform Infrared Spectroscopy was performed at Aberystwyth University's Department of Biological, Environmental and Rural Sciences (IBERS) shortly after the XAS study was completed. It was hypothesised that any changes to the molecular structure would be discernible using FTIR. Spectra were collected in a frequency range from  $5000\text{cm}^{-1}$  to  $700\text{cm}^{-1}$  with a spectral resolution of  $4\text{cm}^{-1}$

The instrument used was the Bruker Equinox 55 Spectrometer, with a MIR source and KBr beamsplitter, the beam exit iris aperture was set to  $7000\mu\text{m}$ . Samples were mounted individually on an Attenuated Total Reflectance (ATR) holder, an add-on accessory from Bruker [27]. This allows the sample to be directly mounted to the holder with no other preparation. The ATR holder is a crystal that is transparent to infrared and the incoming beam reflects at the crystal-sample boundary.

Prior to collecting spectra for a sample, a background spectra was collected for subtraction from the sample spectra. Once collected, the background was automatically subtracted by the instrument control software. The background spectra can be found in A.1.

Sample spectra were collected from 32 scans of each sample, which was then averaged by the software and output as a data file.

# Chapter 4

## Results

### 4.1 XRD

X-ray diffraction was performed at Aberystwyth University to verify the absence of any crystallites in the glass samples, to ensure the samples were amorphous. XRD indicated no crystalline phases in any samples. Diffractograms for MCr and LCr can be found in Appendix B. All samples exhibited a similar line-shape to the diffractogram for HCr01, shown in Figure 4.1.

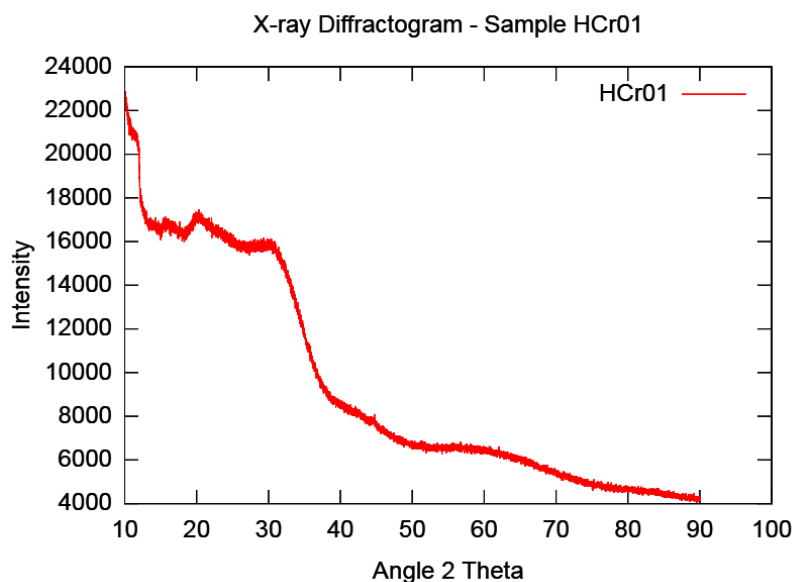


Figure 4.1: X-ray Diffractogram for HCr01 sample after final stage of synthesis

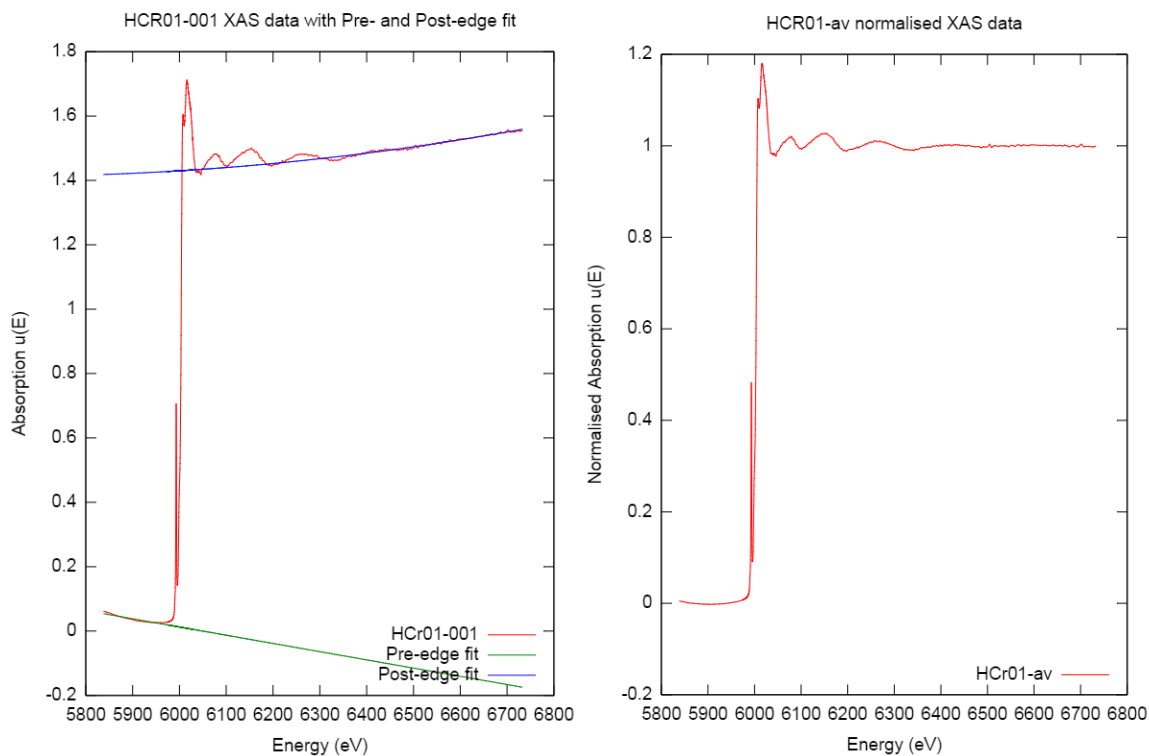
## 4.2 XANES

### 4.2.1 Data Processing

Data treatment, (alignment, averaging, normalisation and background removal) were performed using the IFEFFIT suite, specifically Athena.

Intensity normalisation is achieved through linear and polynomial regression to two areas of the data - the pre-edge and the post-edge respectively. The pre-edge line is regressed in the region from 149 to 29 eV below the selected ionisation energy  $E_0$  (in this case 5998 eV). A third order polynomial was regressed to the post-edge region between 151 to 411 eV above  $E_0$ .

Figure 4.2 (a) shows an example of the fitting of the pre- and post-edge lines (linear and polynomial respectively) to the raw XAS data, and Figure 4.2 (b) shows the normalised averaged XAS spectra for HCr01.



(a) Pre and Post edge fit of HCr01-001

(b) Normalised, averaged XAS data for HCr01

Figure 4.2: Initial raw data processing method for HCr01

EXAFS spectra were fitted using theoretical spectra from  $\text{PbCrO}_4$  (Crocoite) for Cr(VI) and  $\text{NaCrSi}_2\text{O}_6$  (Ureyite) for Cr(III) [28]. Fitting was again performed using the IFEFFIT program suite, using Atoms and Artemis. Theoretical paths were calculated using FEFF8.

#### 4.2.2 Pre-edge of HCr Sample Set

For the HCr sample set, a pre-edge peak occurs roughly 15 eV below the main absorption edge, at about 5993.2 eV. This is consistent with the presence of Cr(VI) in the sample[8].

Figure 4.3 shows the pre-edge spectra for the HCr samples. The pre-edge peaks were fitted using the Fityk software, and following background subtraction, three Gaussian peaks were identified at 5991.7, 5993.2, and 5994.3 eV. The 5993.2 eV peak is the main contribution to the pre-edge and this is due to Cr(VI). Figure 4.4 shows the fit for HCr01 and HCr05, the former being unirradiated, and the latter having received the highest proton dose, and a clear increase in the 5993.2 eV peak can be seen.

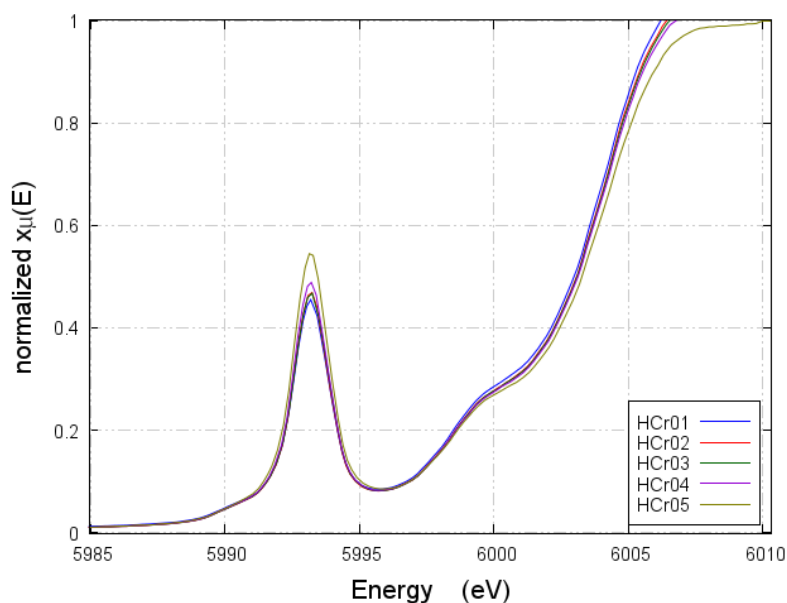


Figure 4.3: Pre-edge XANES spectra for the HCr sample set

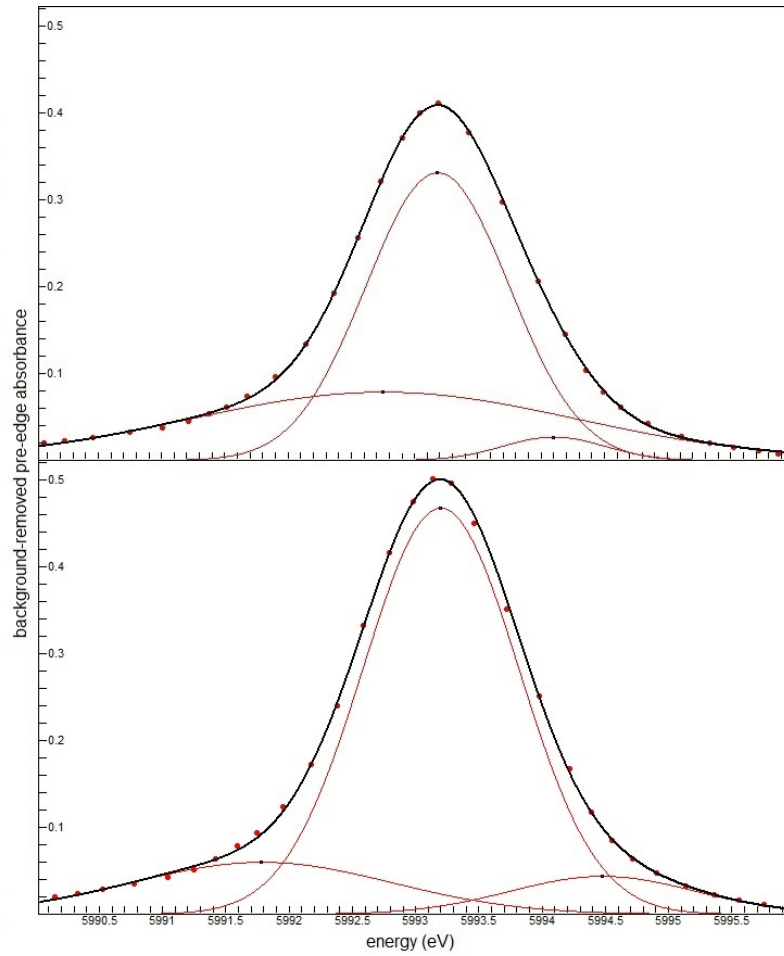


Figure 4.4: Pre-edge peak fitting for HCr01 (top) and HCr05 (bottom). The red points are data, the thick line is the fit and the thin red lines are the contributing Gaussian peaks

### 4.2.3 Pre-edge of MCr Sample Set

In the MCr data set, changes in the pre-edge peak height were observed, but showed no correlation to radiation dose. Figure 4.5 shows the pre-edge XANES spectra for the MCr sample, with the peak of MCr01 and 04 being having greater height than that of 02, 03 and 05.

### 4.2.4 Pre-edge of LCr Sample Set

As with the MCr samples, some small changes in peak height were observed in the XANES pre-edge for the LCr samples. Figure 4.6 shows the XANES pre-edge spec-

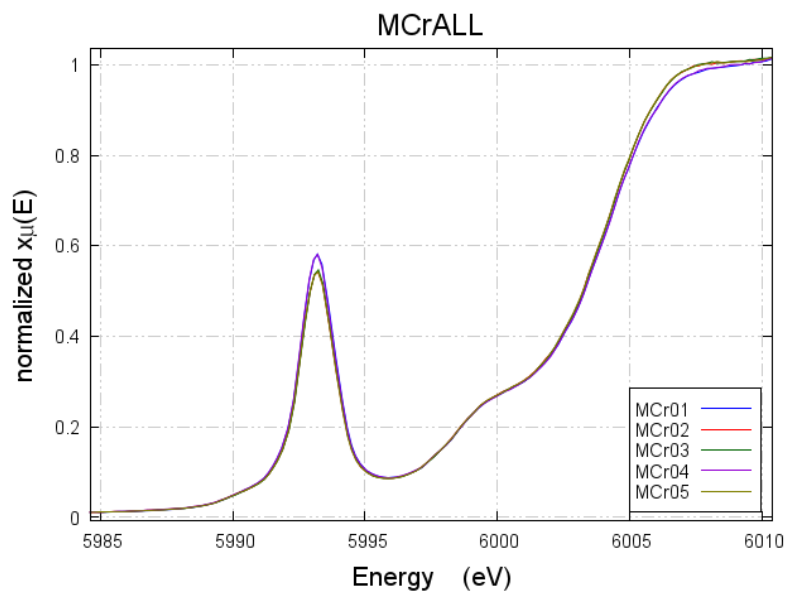


Figure 4.5: Pre-edge XANES spectra for the MCr sample set

tra for LCr01 to 05, and again as with the MCr samples, there appeared to be no correlation between proton dose and the change in the pre-edge peak height.

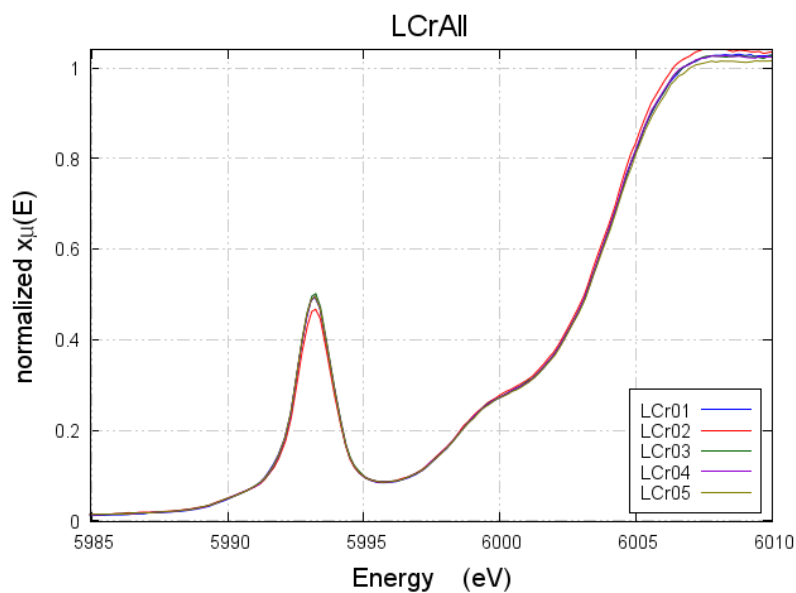


Figure 4.6: Pre-edge XANES spectra for the LCr sample set

### 4.2.5 EXAFS

EXAFS spectra were fitted using Crociote[29][8] and Ureyite[30] as theoretical models and the  $k^3$ -weighted experimental data and corresponding fit can be seen in Figure 4.7 and in Appendix C. Bond distances for Cr-O in octahedral and tetrahedral configuration were calculated. The average Cr(III)-O distance for HCr01 was found to be  $2.03 \pm 0.05\text{\AA}$  which is in good agreement with the  $2\text{\AA}$  distance from literature [8]. The average Cr(VI)-O distance was  $1.67 \pm 0.04\text{\AA}$ , with 3 bonds at  $1.65\text{\AA}$  and 1 at  $1.71\text{\AA}$ . The nearest-neighbour Cr-Cr distance was  $3.02 \pm 0.06\text{\AA}$  in HCr01. Table 4.1 shows the Cr(III)-O, Cr(VI)-O and Cr-Cr bond distances for the HCr sample set.

Sample Name	Cr(III)-O ( $\text{\AA}$ )	Cr(VI)-O ( $\text{\AA}$ )	Cr-Cr ( $\text{\AA}$ )
HCr01	$2.03 \pm 0.05$	$1.67 \pm 0.04$	$3.02 \pm 0.06$
HCr02	$2.05 \pm 0.06$	$1.69 \pm 0.05$	$3.08 \pm 0.08$
HCr03	$2.02 \pm 0.07$	$1.67 \pm 0.05$	$3.05 \pm 0.07$
HCr04	$2.04 \pm 0.06$	$1.68 \pm 0.04$	$3.08 \pm 0.09$
HCr05	$2.01 \pm 0.02$	$1.66 \pm 0.03$	$3.16 \pm 0.06$
MCr01	$2.04 \pm 0.06$	$1.67 \pm 0.05$	$3.15 \pm 0.06$
MCr02	$2.03 \pm 0.05$	$1.66 \pm 0.05$	$3.14 \pm 0.05$
MCr03	$2.05 \pm 0.06$	$1.67 \pm 0.05$	$3.16 \pm 0.07$
MCr04	$2.02 \pm 0.03$	$1.65 \pm 0.03$	$3.12 \pm 0.04$
MCr05	$2.07 \pm 0.08$	$1.69 \pm 0.07$	$2.91 \pm 0.17$
LCr01	$1.98 \pm 0.02$	$1.61 \pm 0.01$	$3.02 \pm 0.06$
LCr02	$2.03 \pm 0.04$	$1.66 \pm 0.03$	$3.12 \pm 0.03$
LCr03	$2.04 \pm 0.05$	$1.67 \pm 0.04$	$3.12 \pm 0.04$
LCr04	$2.06 \pm 0.07$	$1.69 \pm 0.06$	$3.16 \pm 0.07$
LCr05	$2.06 \pm 0.07$	$1.68 \pm 0.06$	$2.87 \pm 0.21$

Table 4.1: Bond distances for the HCr Sample set

### 4.3 FTIR

The obtained FTIR spectra for HCr, MCr and LCr are shown below in Figures 4.8, 4.9, 4.10 respectively. An offset has been applied to each sample's spectra for clarity (left) with the overlaid spectra shown on the right.



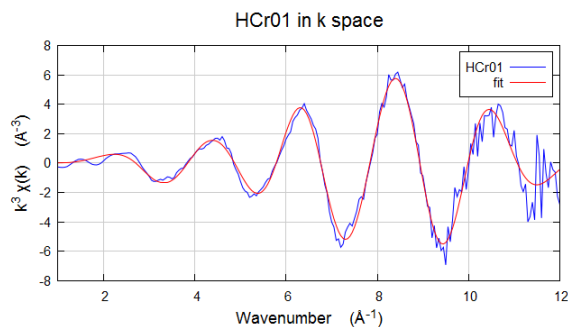


Figure 4.7: Cr K-edge experimental  $k^3$ -weighted EXAFS and fit (smooth line) for HCr01.

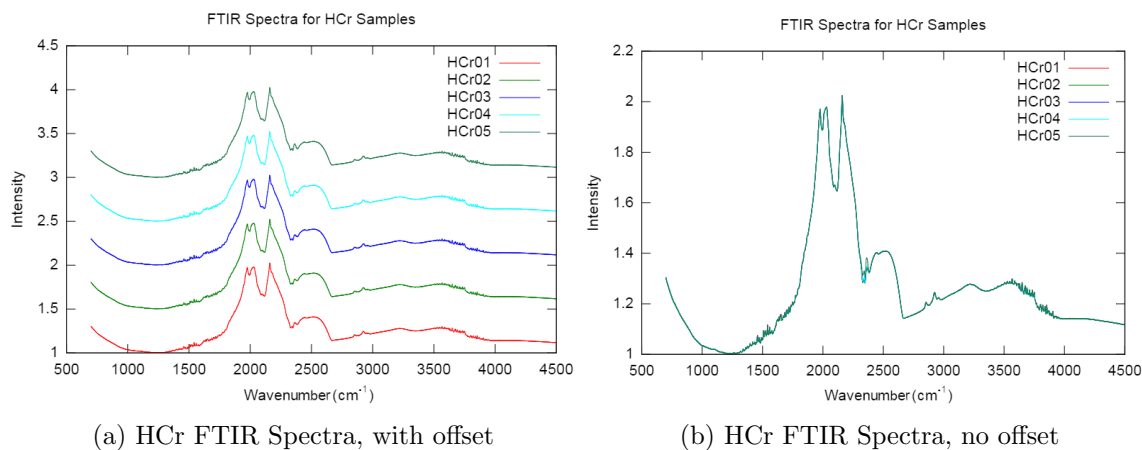


Figure 4.8: FTIR Spectra for the HCr sample set

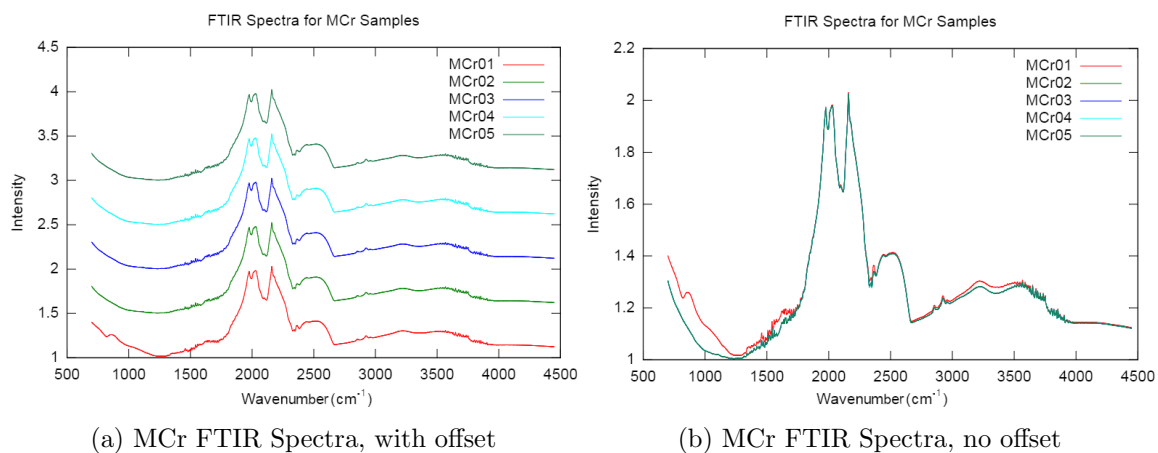


Figure 4.9: FTIR Spectra for the MCr sample set

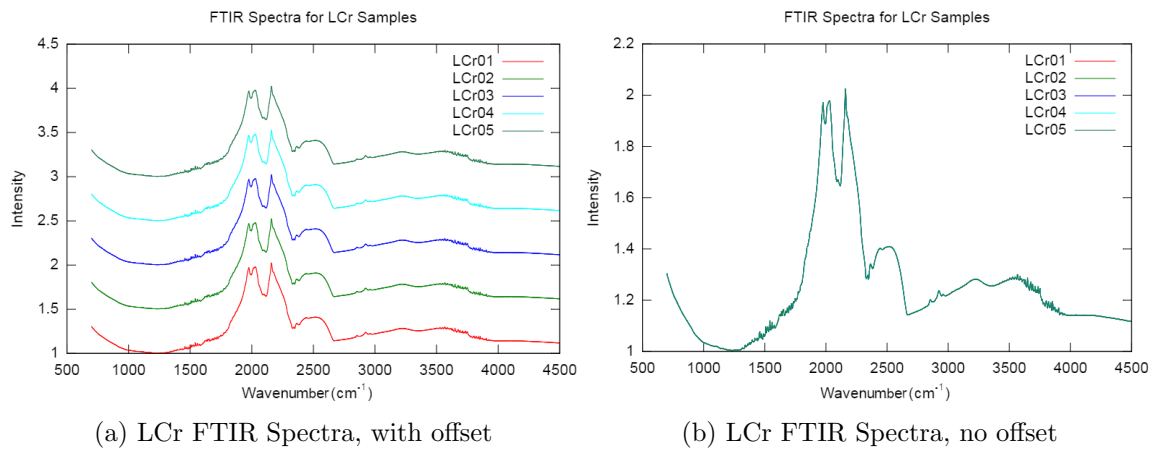


Figure 4.10: FTIR Spectra for the LCr sample set

# Chapter 5

## Discussion

The general line shape of the XANES spectra obtained at beamline 20-BM-B are consistent for samples with a combination of Cr(III) and Cr(VI). All samples in the HCr, MCr, and LCr sets have the same line shape, with varying pre-edge peak heights. This indicates a changing amount of Cr(VI), attributed to proton irradiation of the samples.

The presence of the pre-edge peak in the XANES spectra of all the chromium samples confirms the presences of tetrahedral Cr(VI)O<sub>4</sub>. This arises from a bound-state 1s to 3d transition. In the noncentrosymmetric Cr(VI)O<sub>4</sub> (ie. the tetrahedral structure has no inversion centre), this transition is allowed due to a mixing of 3d and 2p orbitals. In octahedral Cr(III)O<sub>6</sub>, this transition is forbidden due to the centre of symmetry of the molecule. Some very weak features may be present from Cr(III) in the pre-edge due to 1s to 3d(*t<sub>2g</sub>*) and 3d(*e<sub>g</sub>*) electronic transitions at about 5990.5 and 5993.5 eV, which corresponds to the crystal field splitting of the 3d levels in octahedral chromium.

### 5.0.1 XAS of HCr, MCr and LCr

#### 5.0.1.1 HCr

The pre-edge peak for the HCr sample set showed a clear increase in peak height as radiation dose increased. This was further confirmed with analysis of the fitted data,

with the total area under the pre-edge, from 5989 to 5996.5eV, increasing with higher radiation doses (Table 5.1) This would indicate a change in the ratio of octahedral Cr(III) to tetrahedral (VI) chromium. The relative change from HCr01 to HCr05 is a 19.49 percent increase.

Sample Name	Peak Area
HCr01	0.8001
HCr02	0.8004
HCr03	0.8143
HCr04	0.8380
HCr05	0.9561

Table 5.1: Integrated Total Area under the pre-edge peak

#### 5.0.1.2 MCr and LCr

The MCr and LCr sample sets showed some signs of damage existing in the pre-edge peak, but there was no apparent correlation with increasing dose of protons. Whilst the XANES experiments were carried out, attempts were made to minimise added damage caused by the X-ray beam itself. Photoreduction of iron in silicate glasses has been shown to be caused by X-ray beams when the concentration of iron in the glass is below a critical level[31]. This would explain why the MCr and LCr samples showed damage that did not correspond with the proton dose, as they were most likely damaged by the beam itself.

The method used to minimise damage was to take an single XANES scan at a certain physical point on the sample, then move the sample in the beam once the scan had completed. This was repeated for 6 sites on the sample (the size of the sample combined with the width of the beam limited the number of unique spots available on the sample) and then the scans were averaged. For some LCr samples, a number of areas of the sample showed signs of minor colour change due to the incoming X-ray beam. Being as each scan starts at energy below the edge, it is possible that by the time the scan reached higher beam energies, some damage had occurred to the sample.

Figure 5.1 shows the difference between the averaged and individual scans ( $\mu(E)$  against beam Energy) for the MCr01 sample (All other samples can be found in Appendix D). It shows that for lower beam energy, from 5830eV to just above 6400eV, the difference between the average and an individual scan is noise, but as the beam energy increases beyond 6400eV, a clear separation starts to emerge from scan to scan.

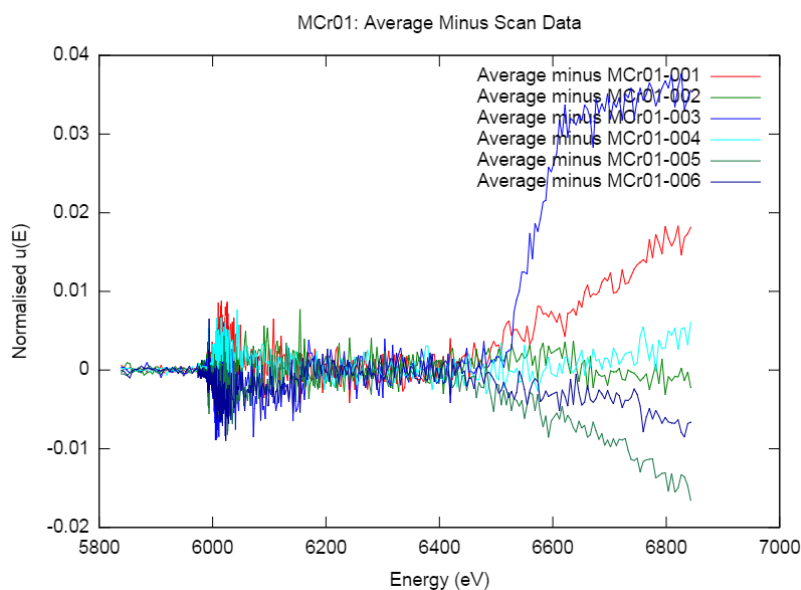


Figure 5.1: MCr02 chart showing difference between individual scans and the average of all six scans

This divergent effect is seen in all samples, and does not appear to correlate with proton dose. There are several potential causes for this effect that would require further investigation:

- This may point towards beam damage being caused to the sample during the scan, as the sample has been exposed to the beam for longer by the time higher energies are reached.
- The sample could potentially be inhomogeneous from site to site, which would be a result of the synthesis process.

- The divergent effect at higher energies may be as a result of the amorphous nature of the glass samples. At higher energies past the absorption edge, secondary multiple scattering effects may begin to dominate the data [32] which would result in some differences from scan to scan.

Several samples showed darkened rectangular areas where the beam had been impinging on the sample during a scan. In order to reduce this effect of damage further, the use of larger samples that could be moved continuously in the X-ray beam during a single would be more appropriate. This would be acceptable as the XANES scans are not site specific if the sample is homogeneous.

### **5.0.2 FTIR**

The results of the FTIR study are somewhat inconclusive. The spectra from the HCr and LCr samples show no significant differences from sample to sample. The hypothesis was that a suggested explanation for the apparent change in relative amount of Cr(VI) to Cr(III) could be that protons from the cyclotron beam combined with O atoms as they passed through the sample. This would lead to the formation of H-O pairs or even H<sub>2</sub>O molecules in the glass matrix. This in turn would result in characteristic peaks in the FTIR spectra, which would show clearly when comparing heavily radiated samples to the un-irradiated sample. However in practise, the use of FTIR as a 'fingerprint' for protons in the sample seems to be quite challenging.

# Chapter 6

## Conclusion

A set of experiments to measure the changes caused by proton radiation to chromium doped silicate glass has been carried out. Following proton irradiation at Birmingham University, UK, Chromium K-edge XANES and EXAFS spectra were collected for 15 samples of chromium doped glasses. The spectra have been analysed to determine the extent of proton radiation damage to silicate glass. FTIR was performed to attempt to identify a possible mechanism of proton damage to the glass.

The oxidation state of chromium in the samples was determined from the pre-edge XANES spectra, and the amount of tetrahedral Cr(VI) increased with increasing proton energy in the high-chromium samples (HCr, 1.5 percent  $\text{Cr}_2\text{O}_3$ ), but for chromium concentrations below this, the synchrotron beam itself may have damaged the glasses.

It is possible (based on similar work [31]) that there is a minimum required concentration of Chromium in the glass for there to be detectable changes to the local structure around the absorber. This is indicated by the results above that show some change to the HCr sample sets, but not in the MCr and LCr sets.

Average bond distances were also calculated for the closest neighbour atoms around the absorber (Cr-Cr, Cr(III)-O and Cr(VI)-O). The results were similar to literature values for these particular bond distance but showed no correlation to proton dose.

In the Introduction to Thesis (Chapter 1), the idea of predicting colour change as

a sample travels through an extra-planetary environment was briefly touched upon. However, this would prove to be difficult due to the varying sources and doses of radiation present in space. A conclusion of this work could be that even with known doses of protons, and well known X-ray energies from a beamline, it is a challenge to characterise the extent of any radiation damage to a sample, so prediction of colour change would be far more difficult.

## 6.1 Further Work

There is scope to build upon the work presented here in several ways. The improvement of data quality could be achieved by taking steps to reduce damage caused by the X-ray beam during the XAS experiment. A larger sample would have meant that the sample could have been slowly moved in the beam continuously, although with the need to take multiple scans for each sample, there would still be some overlap of sampling area from scan to scan.

In order to perform a more quantitative analysis of the XAS spectra, experimental reference samples could be used with known ratios of  $\Sigma \text{Cr(VI)}/\text{Cr}_{total}$  and  $\Sigma \text{Cr(II)}/\text{Cr}_{total}$ , such as crystalline  $\text{Cr}_2\text{O}_3$ ,  $\text{CrO}_2$ ,  $\text{CrO}_3$ [9]. This would allow quantification of the pre-edge peaks in the glass samples, and therefore the Cr(III) and Cr(VI) ratios.



# Appendix A

## FTIR

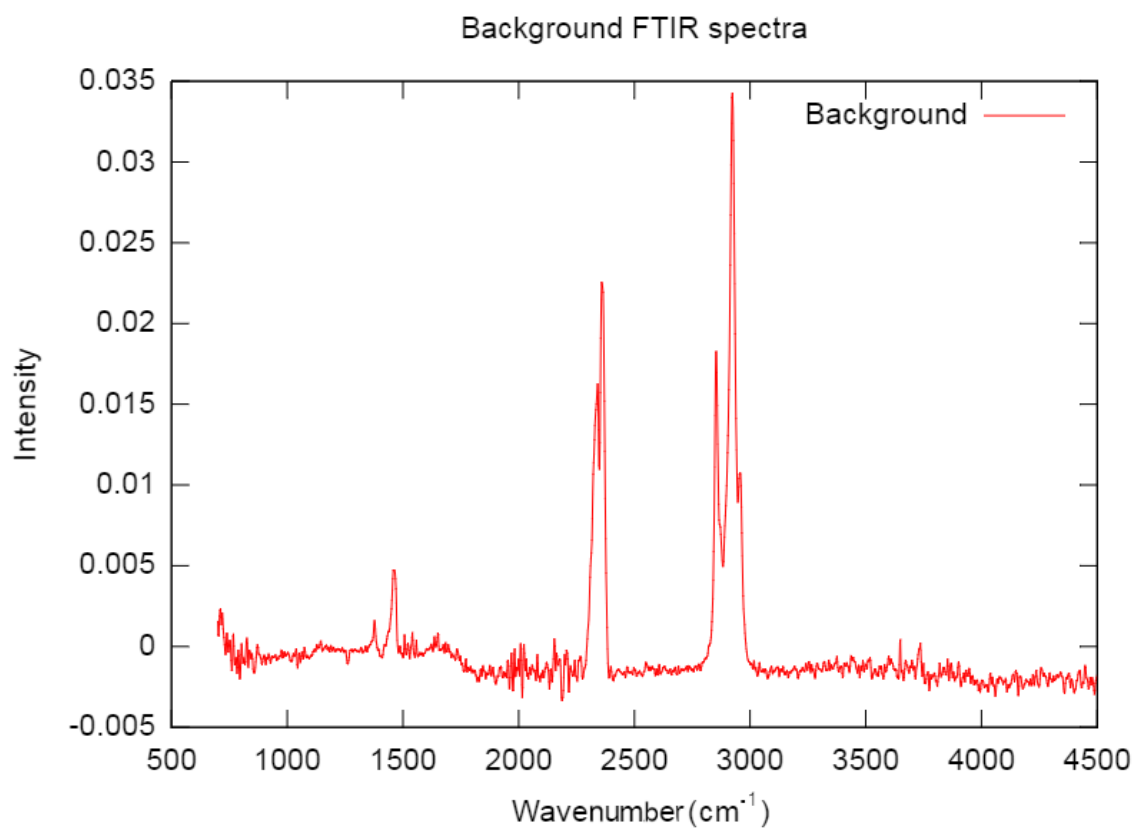


Figure A.1: Background Spectrum for subtraction during FTIR scans

# Appendix B

## XRD

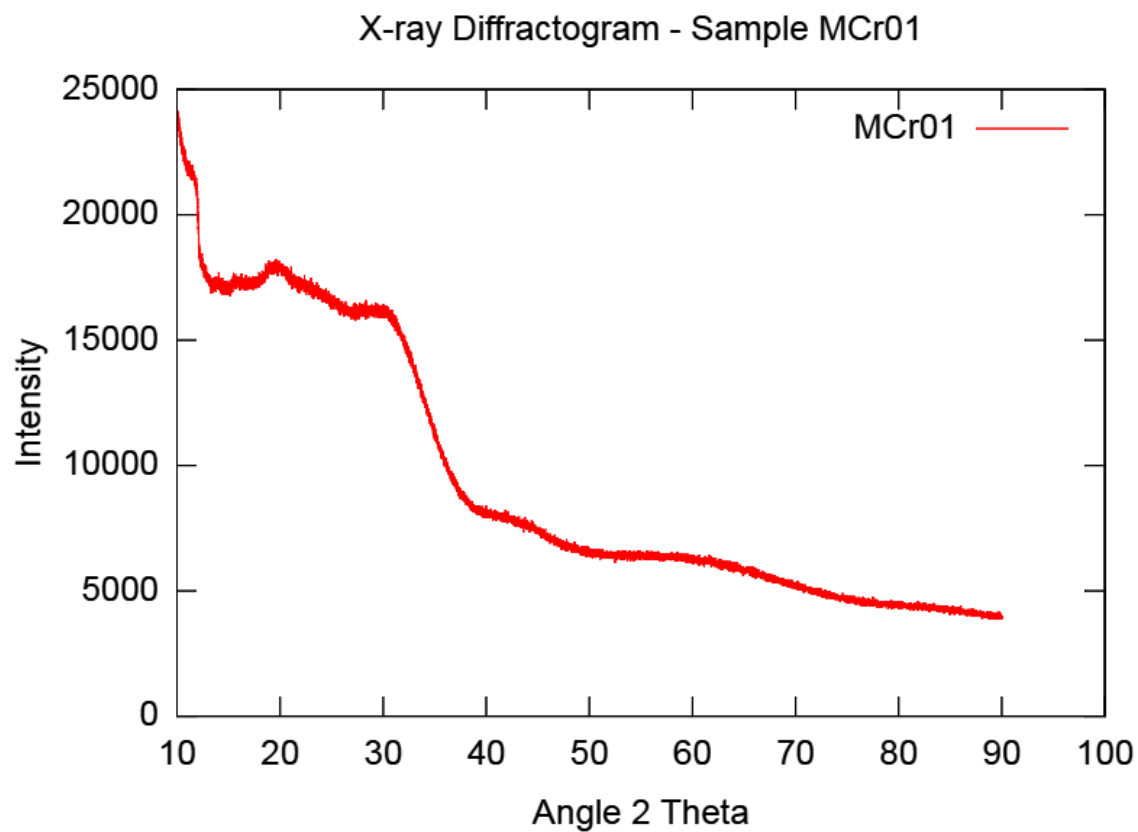


Figure B.1: X-ray Diffractogram for MCr01 sample after final stage of synthesis

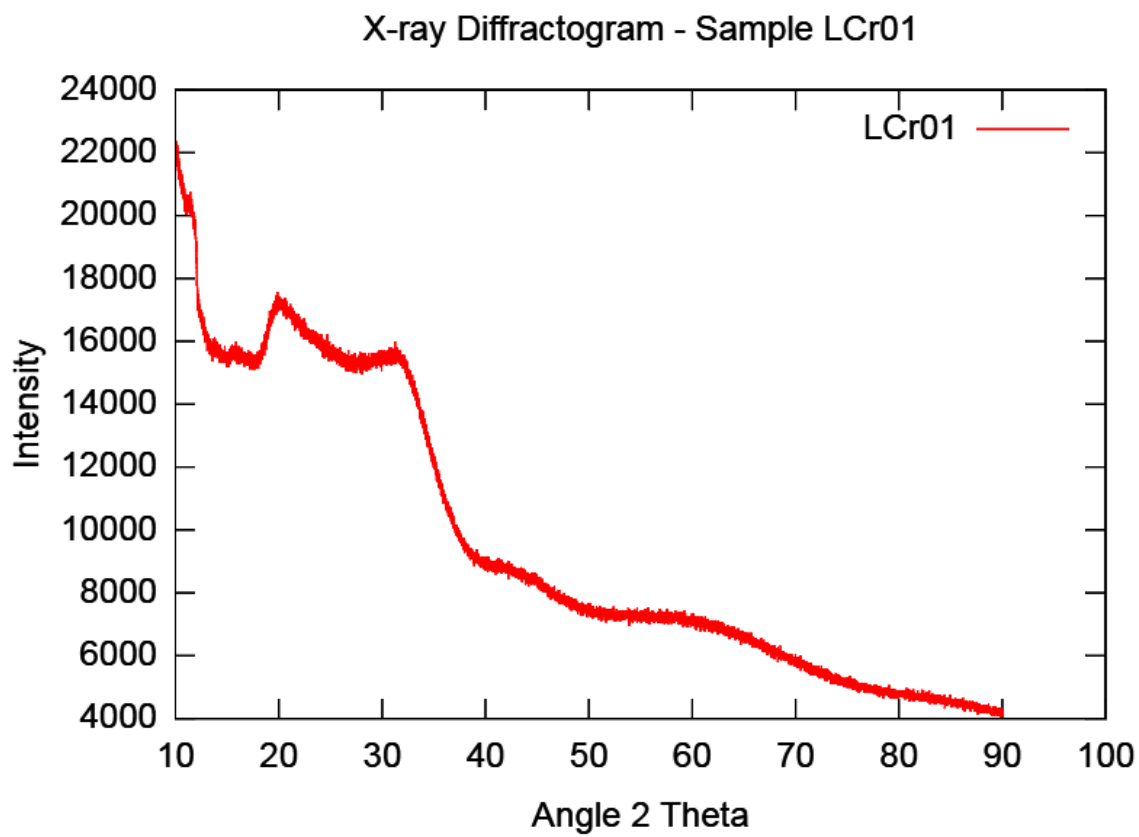
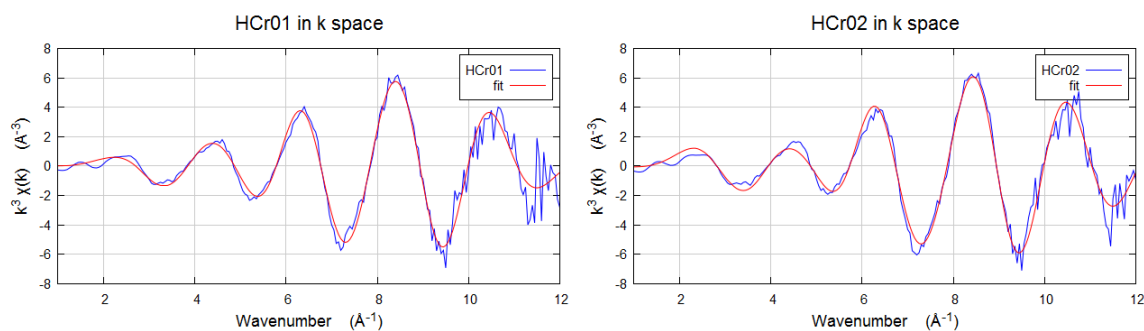


Figure B.2: X-ray Diffractogram for LCr01 sample after final stage of synthesis

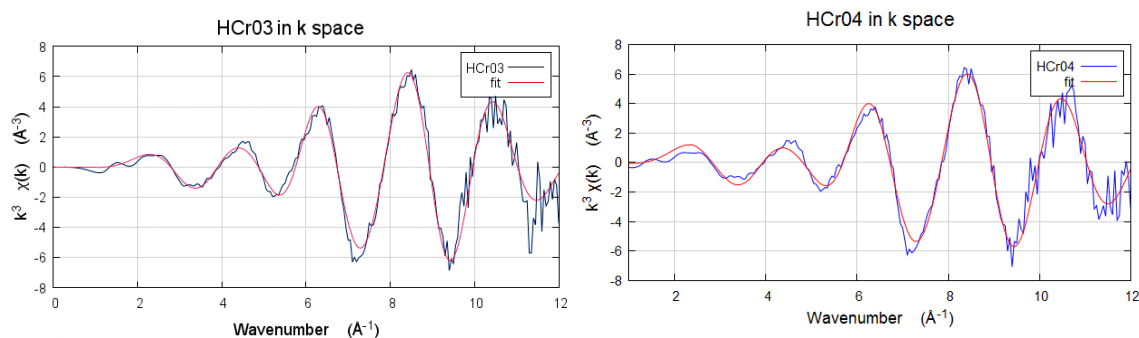
# Appendix C

## EXAFS



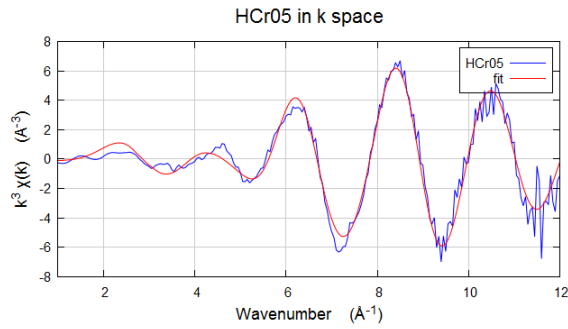
(a) Chromium K-edge experimental  $k^3$ -weighted EXAFS and fit for HCr01 (b) Chromium K-edge experimental  $k^3$ -weighted EXAFS and fit for HCr02

Figure C.1: Cr K-edge experimental  $k^3$ -weighted EXAFS and fit (smooth line) for HCr01 and HCr02.



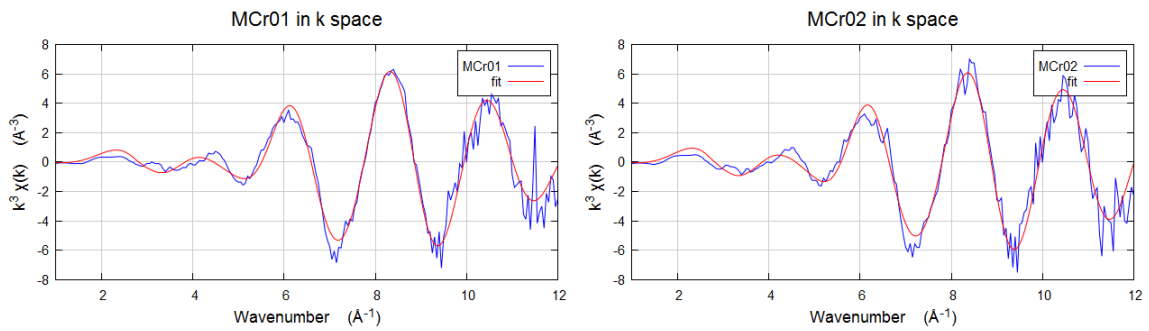
(a) Chromium K-edge experimental  $k^3$ -weighted EXAFS and fit for HCr03 (b) Chromium K-edge experimental  $k^3$ -weighted EXAFS and fit for HCr04

Figure C.2: Cr K-edge experimental  $k^3$ -weighted EXAFS and fit (smooth line) for HCr03 and HCr04.



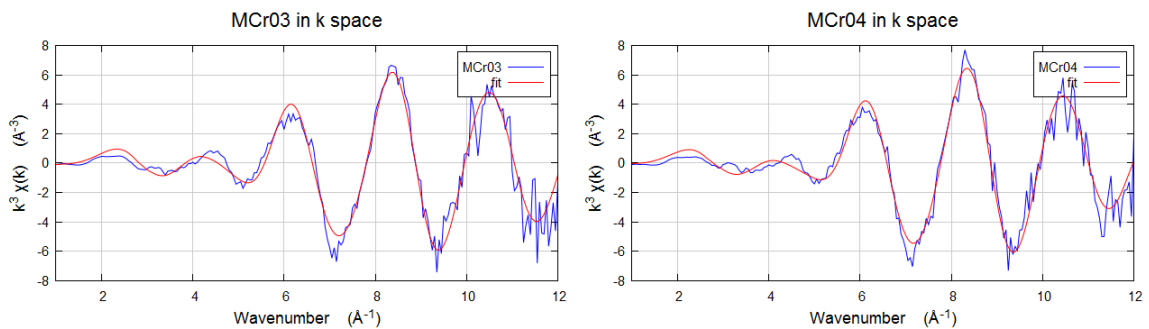
(a) Chromium K-edge experimental  $k^3$ -weighted EXAFS and fit for HCr05

Figure C.3: Cr K-edge experimental  $k^3$ -weighted EXAFS and fit (smooth line) for HCr05.



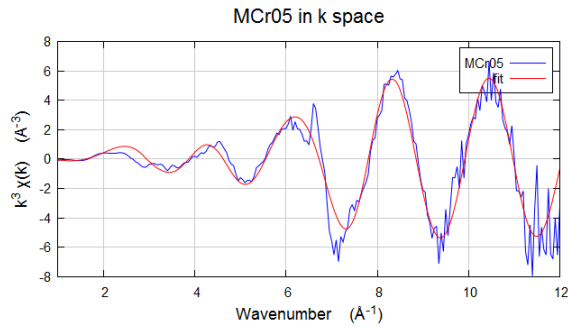
(a) Chromium K-edge experimental  $k^3$ -weighted EXAFS and fit for MCr01 (b) Chromium K-edge experimental  $k^3$ -weighted EXAFS and fit for MCr02

Figure C.4: Cr K-edge experimental  $k^3$ -weighted EXAFS and fit (smooth line) for MCr01 and MCr02.



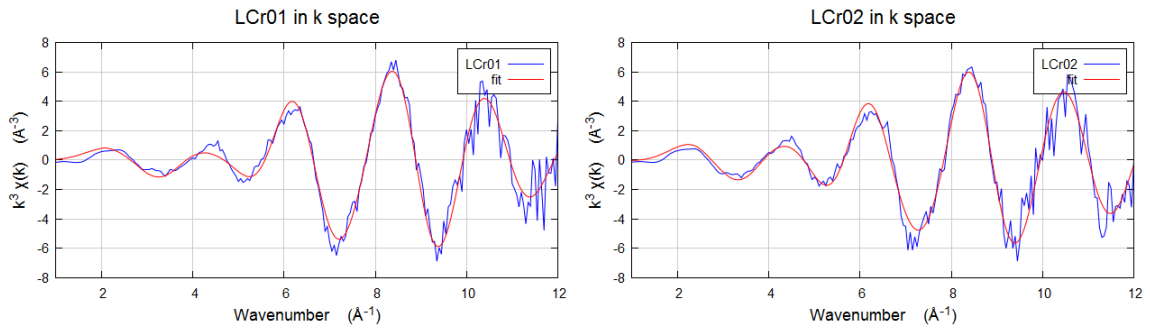
(a) Chromium K-edge experimental  $k^3$ -weighted EXAFS and fit for MCr03 (b) Chromium K-edge experimental  $k^3$ -weighted EXAFS and fit for MCr04

Figure C.5: Cr K-edge experimental  $k^3$ -weighted EXAFS and fit (smooth line) for MCr03 and MCr04.



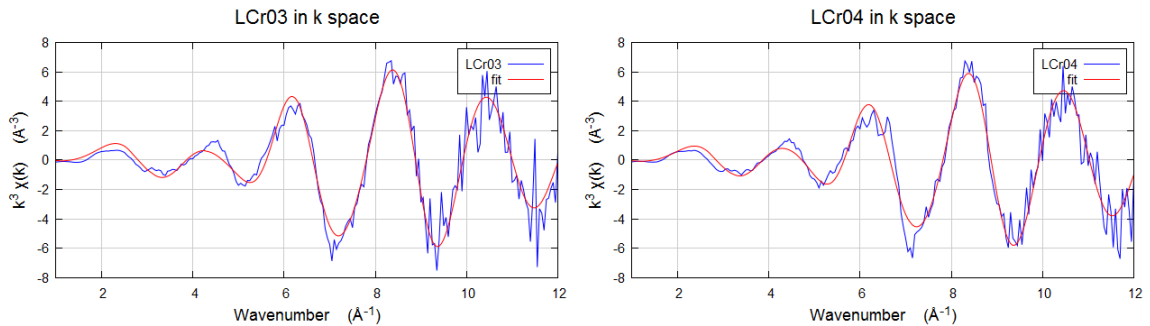
(a) Chromium K-edge experimental  $k^3$ -weighted EXAFS and fit for MCr05

Figure C.6: Cr K-edge experimental  $k^3$ -weighted EXAFS and fit (smooth line) for MCr05.



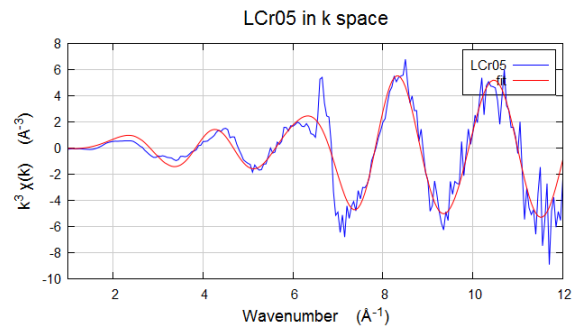
(a) Chromium K-edge experimental  $k^3$ -weighted EXAFS and fit for LCr01 (b) Chromium K-edge experimental  $k^3$ -weighted EXAFS and fit for LCr02

Figure C.7: Cr K-edge experimental  $k^3$ -weighted EXAFS and fit (smooth line) for LCr01 and LCr02.



(a) Chromium K-edge experimental  $k^3$ -weighted EXAFS and fit for LCr03 (b) Chromium K-edge experimental  $k^3$ -weighted EXAFS and fit for LCr04

Figure C.8: Cr K-edge experimental  $k^3$ -weighted EXAFS and fit (smooth line) for LCr03 and LCr04.



(a) Chromium K-edge experimental  $k^3$ -weighted EXAFS and fit for LCr05

Figure C.9: Cr K-edge experimental  $k^3$ -weighted EXAFS and fit (smooth line) for LCr05.

# Appendix D

## XAS Noise

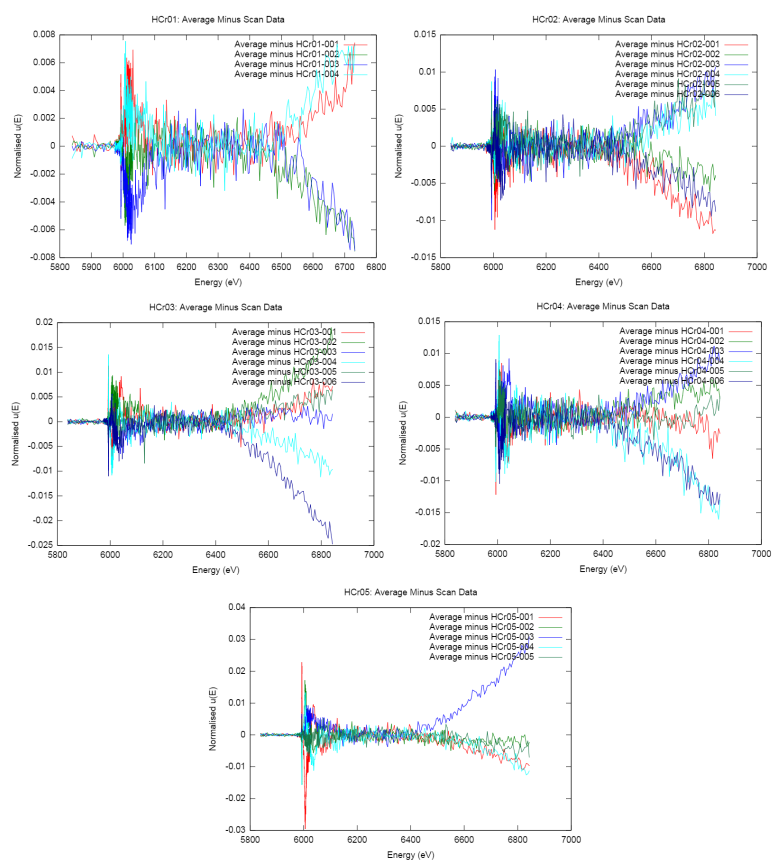


Figure D.1: Averaged  $\mu(E)$  vs Energy minus Individual Scan  $\mu(E)$  vs for the HCr sample set.



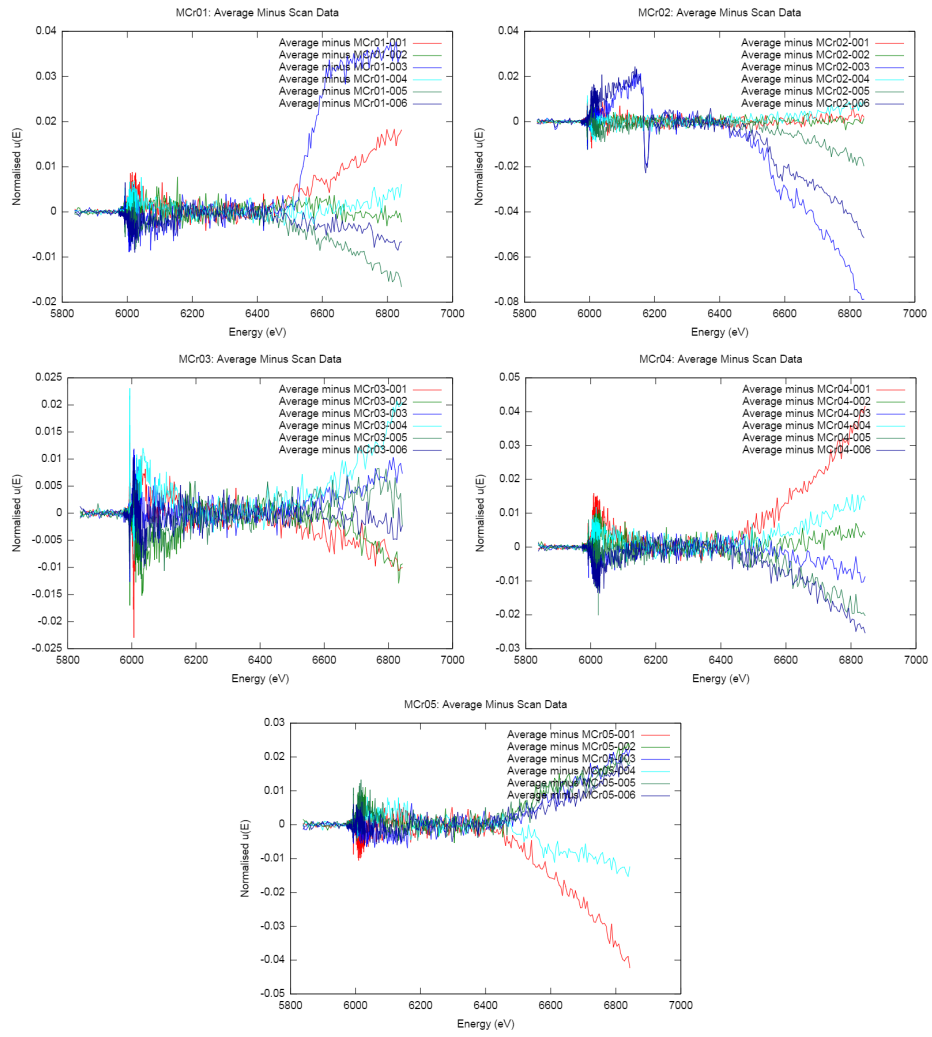


Figure D.2: Averaged  $\mu(E)$  vs Energy minus Individual Scan  $\mu(E)$  vs for the MCr sample set.

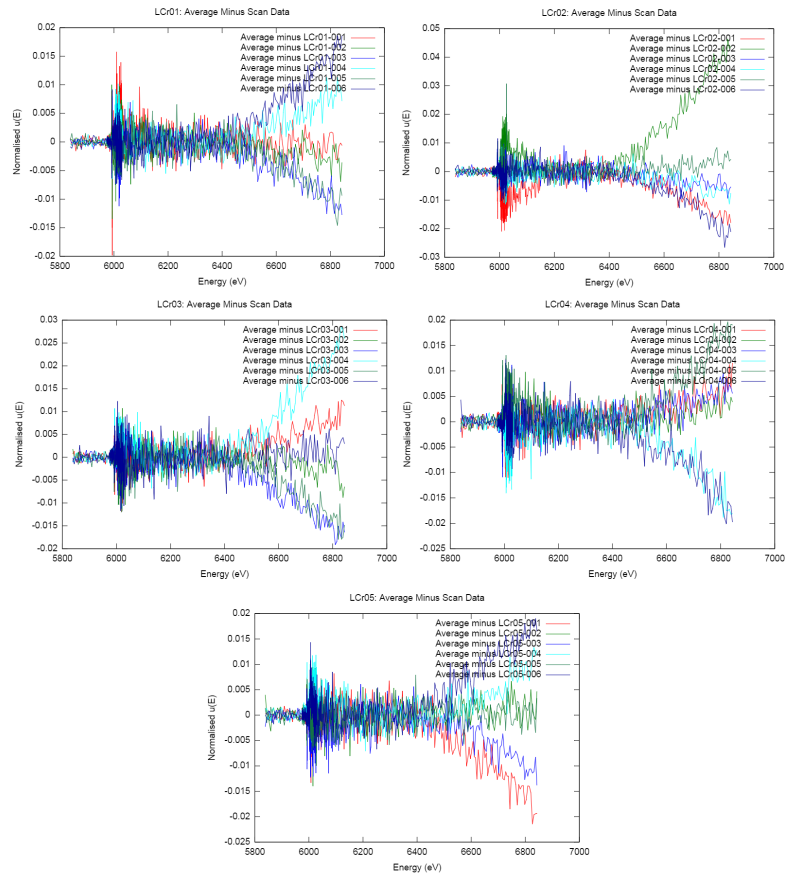


Figure D.3: Averaged  $\mu(E)$  vs Energy minus Individual Scan  $\mu(E)$  vs for the LCr sample set.

# Bibliography

- [1] A. Coates, A. Griffiths, C. Leff, N. Schmitz, D. Barnes, J.-L. Josset, B. Hancock, C. Cousins, R. Jaumann, I. Crawford, G. Paar, and A. Bauer, “Lunar PanCam: Adapting ExoMars PanCam for the ESA Lunar Lander,” *Planetary and Space Science*, vol. 74, pp. 247–253, Dec. 2012.
- [2] G. G. Sedano, “Silica.” [Online; accessed 15-June-2015].
- [3] V. Petkov, S. J. L. Billinge, S. D. Shastri, and B. Himmel, “Polyhedral units and network connectivity in calcium aluminosilicate glasses from high energy X-ray diffraction,” *Phys. Rev. Lett.*, vol. 85, p. 3436, 2000.
- [4] M. Wilke, G. M. Partzsch, R. Bernhardt, and D. Lattard, “Determination of the iron oxidation state in basaltic glasses using XANES at the K-edge,” *Chemical Geology*, vol. 213, pp. 71–87, Dec. 2004.
- [5] O. Villain, G. Calas, L. Gaiosy, L. Cormier, and J.-L. Hazemann, “XANES Determination of Chromium Oxidation States in Glasses: Comparison With Optical Absorption Spectroscopy,” *Journal of the American Ceramic Society*, vol. 90, pp. 3578–3581, Nov. 2007.
- [6] O. Villain, L. Gaiosy, and G. Calas, “Spectroscopic and structural properties of Cr<sup>3+</sup> in silicate glasses: Cr<sup>3+</sup> does not probe the average glass structure,” *Journal of Non-Crystalline Solids*, vol. 356, pp. 2228–2234, Sept. 2010.

- [7] S. Bajt, S. B. Clark, S. R. Sutton, M. L. Rivers, and J. V. Smith, "Synchrotron X-ray Microprobe Determination of Chromate Content Using X-ray Absorption Near-Edge Structure," *Analytical Chemistry*, vol. 65, no. 14, pp. 1800–1804, 1993.
- [8] M. L. Peterson, G. E. Brown, G. a. Parks, and C. L. Stein, "Differential redox and sorption of Cr (III/VI) on natural silicate and oxide minerals: EXAFS and XANES results," *Geochimica et Cosmochimica Acta*, vol. 61, pp. 3399–3412, Aug. 1997.
- [9] Y. G. Choi, K. H. Kim, Y. S. Han, and J. Heo, "Oxidation state and local coordination of chromium dopant in soda-lime-silicate and calcium-aluminate glasses," *Chemical Physics Letters*, vol. 329, no. 5, pp. 370–376, 2000.
- [10] A. Berry and H. O'Neill, "A XANES determination of the oxidation state of chromium in silicate glasses," vol. 89, pp. 790–798, 2004.
- [11] L. Zanella, F. Casadio, K. a. Gray, R. Warta, Q. Ma, and J.-F. Gaillard, "The darkening of zinc yellow: XANES speciation of chromium in artist's paints after light and chemical exposures," *Journal of Analytical Atomic Spectrometry*, vol. 26, no. 5, p. 1090, 2011.
- [12] D. College, "Cyclotron diagram." [Online; accessed 15-May-2016].
- [13] J. Yano and V. K. Yachandra, "X-ray absorption spectroscopy," *Photosynthesis Research*, vol. 102, no. 2, pp. 241–254, 2009.
- [14] S. M. Heald, D. L. Brewster, E. A. Stern, K. H. Kim, F. C. Brown, D. T. Jiang, E. D. Crozier, and R. A. Gordon, "XAFS and micro-XAFS at the PNC-CAT beamlines," *Journal of Synchrotron Radiation*, vol. 6, pp. 347–349, May 1999.

- [15] A. Filipponi, A. D. Cicco, and V. Madonna, “X-ray absorption spectroscopy and n-body distribution functions in condensed matter. I. Theory,” vol. 52, no. 21, pp. 122–134, 1995.
- [16] A. Filipponi, A. D. Cicco, and V. Madonna, “X-ray-absorption spectroscopy and n-body distribution functions in condensed matter. II. Data analysis and applications,” vol. 52, no. 21, pp. 135–149, 1995.
- [17] L. Galois, G. Calas, and M. A. Arrio, “High-resolution XANES spectra of iron in minerals and glasses : structural information from the pre-edge region,” pp. 307–319, 2001.
- [18] A. Berry and O. Hugh, “XANES calibrations for the oxidation state of iron in a silicate glass,” vol. 88, pp. 967–977, 2003.
- [19] E. Cottrell, K. A. Kelley, A. Lanzirotti, and R. A. Fischer, “High-precision determination of iron oxidation state in silicate glasses using XANES,” *Chemical Geology*, vol. 268, pp. 167–179, Nov. 2009.
- [20] W. M. Doyle, “Principles and applications of Fourier transform infrared ( FTIR ) process analysis,” *Process Control and Quality*, vol. 2, pp. 11–41, 1992.
- [21] B. Fischer and K. Gerth, “Platinum for Glass Making at Jena,” *Platinum Metals Review*, vol. 38, no. 2, pp. 74–82, 1994.
- [22] B. Schmidt, F. Holtz, and J.-M. Bény, “Incorporation of H<sub>2</sub> in vitreous silica, qualitative and quantitative determination from Raman and infrared spectroscopy,” *Journal of Non-Crystalline Solids*, vol. 240, pp. 91–103, Oct. 1998.
- [23] Y. Makhkhas, S. Aqdim, and E. Sayouty, “Study of sodium-chromium-iron-phosphate glass by XRD, IR, Chemical Durability and SEM,” *Technical Pro-*

*ceedings of the 2013 NSTI Nanotechnology Conference and Expo, NSTI-Nanotech 2013*, vol. 1, no. August, pp. 1–6, 2013.

- [24] J. F. Ziegler, J. Biersack, and U. Littmark, “The Stopping and Range of Ion in Matter,” 1985.
- [25] U. of Birmingham Nuclear Physics Research Group, “The mc40 cyclotron.” [Online; accessed 15-May-2016].
- [26] B. M. Weon, J. T. Kim, J. H. Je, J. M. Yi, S. Wang, and W. K. Lee, “Colloid coalescence with focused x rays,” *Physical Review Letters*, vol. 107, no. 1, pp. 1–4, 2011.
- [27] Bruker Optics, “Application Note AN # 79 Attenuated Total Reflection ( ATR ) a versatile tool for FT-IR spectroscopy Refractive index,” 2011.
- [28] M. Newville, “The atoms.inp archive - a collection of crystallographic data for use in xafs analysis.” [Online; accessed 15-May-2016].
- [29] K. S. Knight, “A high temperature structural phase transition in crocoite (PbCrO<sub>4</sub>) at 1068 K: crystal structure refinement at 1073 K and thermal expansion tensor determination at 1000 K,” *Mineralogical Magazine*, vol. 64, no. 2, pp. 291–300, 2000.
- [30] M. Cameron, S. Sueno, C. T. Prewitt, and J. J. Papike, “High-Temperature of Acmite , Diopside , Grystal Ghemistry and Ureyite,” *American Mineralogist*, vol. 58, pp. 594–618, 1973.
- [31] A. G. Whittington, P. Richet, D. B. Dingwell, P. Gonçalves Ferreira, D. de Ligny, O. Lazzari, A. Jean, O. Cintora Gonzalez, and D. Neuville, “Photoreduction of iron by a synchrotron X-ray beam in low iron content soda-lime silicate glasses,” *Chemical Geology*, vol. 346, pp. 106–112, 2013.

- [32] W. E. Jackson, F. Farges, M. Yeager, P. a. Mabrouk, S. Rossano, G. a. Waychunas, E. I. Solomon, and G. E. Brown, “Multi-spectroscopic study of Fe(II) in silicate glasses: Implications for the coordination environment of Fe(II) in silicate melts,” *Geochimica et Cosmochimica Acta*, vol. 69, pp. 4315–4332, Sept. 2005.